Geodetic observations during the 2009 eruption of Redoubt Volcano, Alaska

Ronni Grapenthin *, Jeffrey T. Freymueller, Alexander Max Kaufman

Geophysical Institute, University of Alaska Fairbanks, 903 Koyukuk Drive, P.O. Box 757320, Fairbanks, AK 99775-7320, USA

A B S T R A C T

In March 2009 Redoubt Volcano, about 160 km to the SW of Anchorage, Alaska, began its most recent explosive eruption. Deformation induced by this event was recorded by a GPS campaign network consisting of 14 benchmarks, which had been established in 1991 after the previous eruption. The network was partially reoccupied in 2001 and 2008 and no volcanic deformation was detected during that period. In response to precursory unrest starting in January 2009, the Alaska Volcano Observatory temporarily deployed continuously recording GPS instruments at four of the campaign benchmarks only days before the onset of explosive activity in March 2009.

The only GPS instrument recording continuously during the months prior to the eruption was the Plate Boundary Observatory (PBO) station AC17, about 28 km northeast of the volcano's summit. Data from this station reveals subtle motion radially outward from the volcano beginning as early as May 2008, which reversed with the onset of explosive activity.

Using simple analytical models we link the precursory activity to a point source intrusion of $0.0194\,^{0.0092}_{0.0340}$ km^3 in volume at $13.50\,^{10.17}_{17.33}$ km below sea level (bsl, superscripts and subscripts refer to upper and lower ends of confidence intervals at the 95% level). During the explosive phase about $0.05\,^{0.028}_{>0.1}$ km^3 of magma was evacuated from a prolate spheroid with its centroid at $9.17\,^{6.92}_{15.17}$ km bsl, a semimajor axis of $4.50\,^{1.25}_{>10.00}$ km length and a semi-minor axis of $0.475\,^{0.3}_{>4.0}$ km. The effusive activity is inferred to come from the same source, decreasing in volume by $0.0167\,^{0.0106}_{0.0228}$ km^3.

Including observations from seismology and petrology, we hypothesize a mid-crustal two reservoir system with material sourced from > 20 km flowing in at about 13.5 km depth and reheating residual material in the proposed spheroid. The mixture migrated to shallower depth (2–4.5 km bsl) and reheated material there. As this residual magma erupted, it was replaced by the material from the spheroidal reservoir at 7–11.5 km depth, which renders the shallow source undetectable for geodetic instruments.

In addition to long term displacements we investigate sub-daily kinematic positioning solutions and find that large, short-term positioning offsets correlate with large explosive events. Spikes in phase residuals plotted along the sky tracks of individual satellites can be related to individual plumes given favorable satellite–station-geometry, which may be of use in volcano monitoring.

1. Introduction

Redoubt Volcano lies in the Cook Inlet region on the northeastern segment of the Aleutian arc. It is about 160 km southwest of Anchorage inside the Lake Clark National Park and Preserve (Fig. 1, left) and about 400 km northwest of the Aleutian Megathrust (Fig. 1 inset), where the Pacific Plate subducts beneath Alaska. The last eruption prior to the 2009 event occurred in 1989–1990 and is described in detail in Miller and Chouet (1994). The region is volcanically active with historic eruptions at the neighboring volcanoes Augustine and Mt. Spurr.

Mt. Redoubt is a 3108 m high stratovolcano with a diameter of 10–12 km at its base at about 1200–1500 m above sea level. The ice filled summit crater is about 1.5 km in diameter and is breached to the north, which allows Drift Glacier to stretch up to 5 km down slope and into the Drift River Valley. Other smaller glaciers radiate from the summit region and dissect the volcanic edifice (Fig. 1, left). The overall largest mass of ice in the region is the Double Glacier ice cap, which covers Double Glacier Volcano (Reed et al., 1992) on the northern side of the Drift River Valley.

In the years since the 1989–90 eruption, surface deformation studies of volcanoes have made significant contributions to the field of volcanology. We can use simple models to link surface displacements to subsurface motion of material and thus infer knowledge of the plumbing system, displaced volumes and source depths as well as the general state of the volcano. These techniques have been applied successfully to a wide range of volcanoes worldwide (Dzurisin, 2003, and references therein).

At Redoubt Volcano surface deformation is measured with high-precision GPS in a network of 14 geodetic benchmarks. InSAR based studies are generally difficult, because the glaciated, steep terrain affects signal coherence and the strongest deformation signal related to the 2009 eruption spreads over a wide region with an amplitude
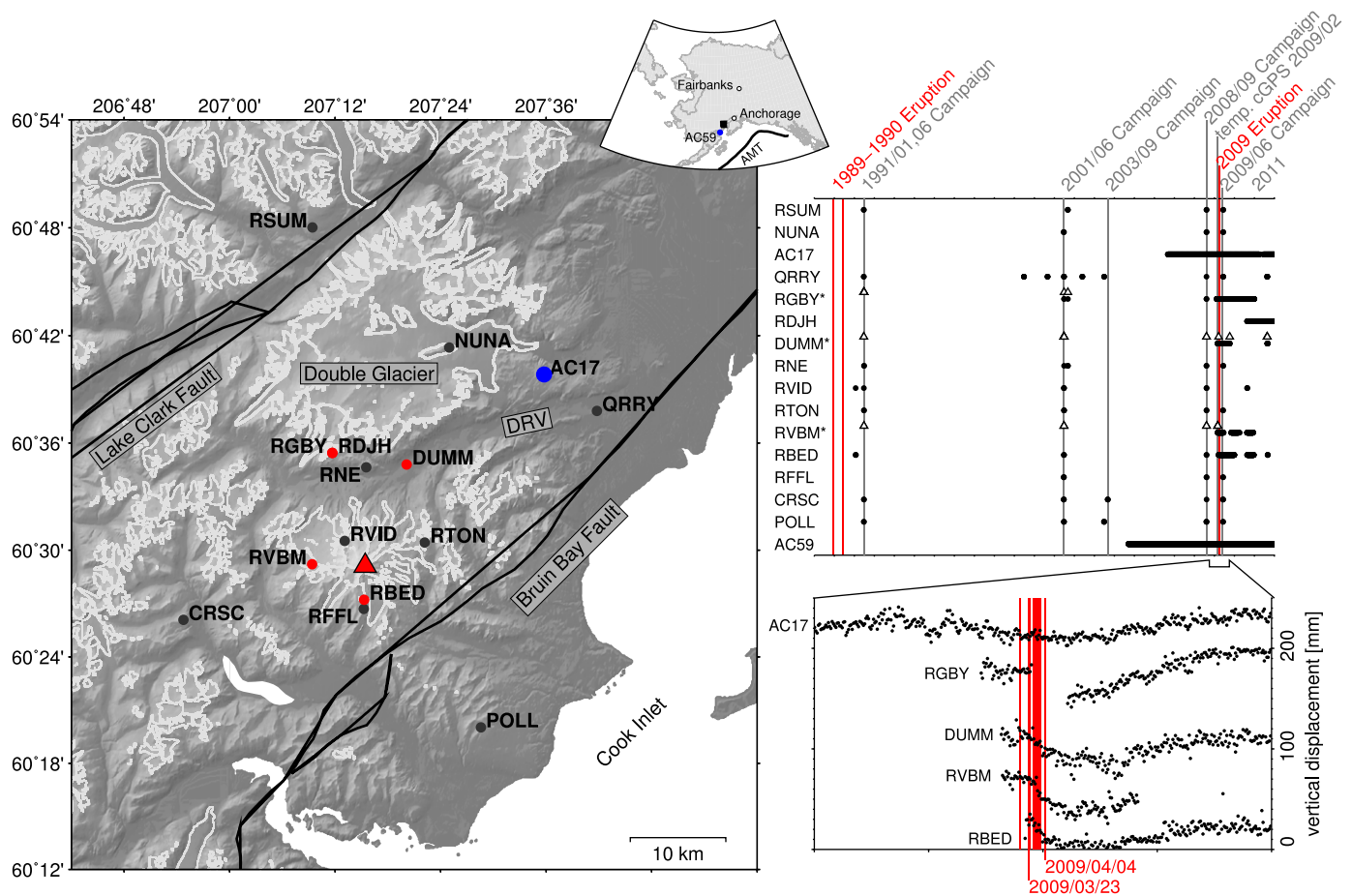
Fig. 1. Regional setting and available GPS data. **Left**: Map of Redoubt area with GPS stations. The red triangle marks Mt. Redoubt. Red circles indicate temporary continuous GPS stations, black circles mark campaign GPS stations, and the blue circle indicates the continuous PBO site AC17. White outlines mark glaciers in the region (Paul, 2010). The Double Glacier ice cap to the north of Redoubt is outlined in gray and labeled; it seems to influence the time series at RGBY located on a cliff above one of its southern outlet glaciers. NUNA is located on a large nunatak that sticks out of the ice. The black lines from SW to NE indicate major faults in the region: Bruin Bay Fault to the south, and Lake Clark Fault north of Redoubt Volcano. DRV labels the mouth of the Drift River Valley. The black square in the inset indicates the location of this detail map. It also shows the location of the PBO site AC59 and the Aleutian Megathrust (AMT). **Right:** Overview of site occupations. Asterisks mark sites with composites of two tied markers. Each dot marks an existing daily positioning solution. Triangles mark occupations of DUMB, RGRB, and RVBR which are tied to DUMM, RGBY and RVBM, respectively. Times of individual campaigns are given on the top and are marked by gray lines. Red lines mark the 1989–1990 eruption and the recent event of 2009. The timescale is linear. The lower right figure is a blow up of the (temporary) continuous stations from the decimal year 2008.75 to 2009.75 and shows vertical displacements for this time period. Vertical red lines indicate individual explosions (Table 1 in Bull and Buurman, this volume). Times are given for the first deformation inducing eruption on March 23, 2009, and the largest and last explosion on April 4th, 2009. (For interpretation of the references to color in this figure legend, the reader is referred to the web version of this article.)

much smaller than the SAR wavelength. From 1991 to 2008, 4 GPS campaigns were carried out, each occupying a set of benchmarks for a few days (Fig. 1). In response to observed changes in activity of the volcano (e.g., Bull and Buurman, this volume) 4 temporary continuous GPS stations (DUMM, RBED, RGBY, RVBM; Fig. 1) were installed several weeks prior to the 2009 eruption.

An overview of the event, summarizing key observations from various disciplines, is given by Bull and Buurman (this volume). They separate the eruption into three distinct phases: precursory (July 2008–15 March 2009), explosive (15 March–04 April 2009), and effusive phase (April 4–July 2009). The precursory phase is characterized by sulfur odors Bull et al., 2012, increased melting of Drift River glacier showing collapse pits (Bleick et al., this volume) and deep seismicity beginning in December 2008 (Power et al., this volume). For the explosive phase, Bull and Buurman (this volume, Fig. 2) describe a complex interplay of dome growth, collapse and explosive activity, and count 28 explosions with plumes reaching up to >18 km above sea level (asl) (Table 1 in Bull and Buurman, this volume). The final, persisting lava dome was extruded during the effusive phase. Its initial rapid growth slowed during the final stage of dome building through lava intrusions into the dome (Bull and Buurman, this volume; Diefenbach et al., this volume).

Here, we present the first geodetic study of Redoubt Volcano and focus on observations during the 2009 eruption. We start with an overview of the geodetic network and data recorded at Redoubt since 1991. We investigate GPS time series for the different phases of the eruption, from which we infer source geometry, location and volume change for each phase of the eruption. Since deep pre-eruptive long period earthquakes indicate migration of material below 20 km depth (Power et al., this volume) and petrologists suggest that the magma of this event was sourced relatively shallow at 2–4.5 km bsl (Coombs et al., this volume), we are particularly interested in the question whether Redoubt presents us with a multi-source system. Furthermore, we investigate whether subdaily, kinematic positioning solutions can resolve any deformation that correlates with explosive activity.

2. GPS data

2.1. GPS network history and site description

The geodetic network at Redoubt Volcano consists of 14 markers (Fig. 1, Table 1); most of these were installed in response to the 1989 eruption and were first occupied during a campaign in 1991.

Table 1
GPS benchmark coordinates. Installation dates (YYYY-MM-DD) represent the earliest available data.

4 Char ID	Lat (deg)	Lon (deg)	Height (m)	Installation date	Dist to Redoubt (km)
RSUM	60.800404	−152.843023	908.4798	1991-06-20	35
NUNA	60.688944	−152.583804	954.2120	1991-06-20	24
QRRY	60.629873	−152.303741	56.1551	1991-06-20	30
RGBY	60.590781	−152.805216	1421.4969	2001-06-25	12
RDJH	60.590764	−152.805241	1422.4000	2010-08-20	12
DUMB	60.579978	−152.664516	230.6017	1991-06-20	11.5
DUMM	60.579923	−152.664469	231.1957	2009-02-27	11.5
RNE_	60.577380	−152.741092	994.2093	1991-06-25	10
RVID	60.508641	−152.781835	1886.6534	1991-01-25	2.4
RTON	60.507123	−152.630164	1358.8424	1991-06-23	7.5
RVBM	60.486809	−152.843623	1646.2630	2009-02-28	4.5
RVBR	60.486866	−152.843663	1646.2310	1991-06-23	4.5
RBED	60.453568	−152.744912	1557.8103	1991-01-25	4.0
RFFL	60.444978	−152.745881	1445.8446	1991-06-23	5.0
CRSC	60.434693	−153.087553	1073.3678	1991-06-22	19
POLL	60.333857	−152.523572	849.9948	1991-06-21	22
West of Cook Inlet					
AC17	60.663902	−152.403846	882.6025	2006-08-31	28
AC59	59.567197	−153.585201	308.5802	2004-09-01	112

The network was reoccupied in 2001, 2008, 2009, and 2010 (Fig. 1, right). No continuous sites were present in the region until 2006, when the Plate Boundary Observatory (PBO) site AC17 was installed about 28 km to the NE of the volcano near the Drift River Oil Terminal. In response to the elevated levels of seismicity at Redoubt Volcano beginning January 2009 (Buurman et al., this volume), the Alaska Volcano Observatory (AVO) converted the campaign sites DUMB, RBED, RVBR, and RGBY to temporary continuous deployments using fixed height mast installations. During this effort RVBM and DUMM were installed as secondary survey marks suitable for deployment with a mast. The original DUMB benchmark could not be found under the late February snow cover and RVBR is a benchmark on a pole, only suitable for use with a tripod. DUMM and RVBM were installed on February 27 and 28, 2009, respectively. The RBED installation did not occur until March 18, 2009; 5 days before the onset of explosive magmatic activity (Fig. 1, right). These sites were equipped with Trimble 5700 receivers and Zephyr Geodetic antennas. The station on Gorby's Summit, RGBY, was installed on February 10, 2009 and equipped with a Trimble NetRS receiver and a Zephyr Geodetic antenna. This was the only digitally telemetered station during the 2009 eruption as it is co-located with the telemetered seismic station RDJH (Buurman et al., this volume). Data from the other temporary
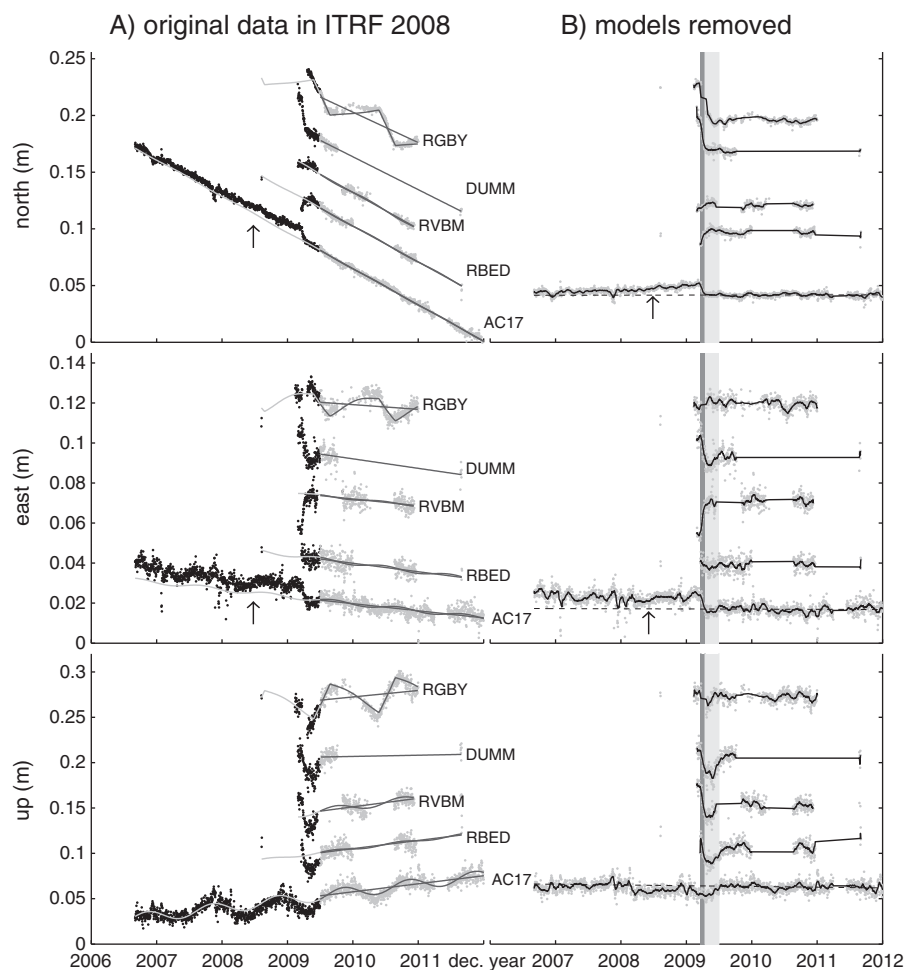
Fig. 2. Original time series of positions in ITRF 2008 (A) and detrended data (B) from 2006 to 2012. The rows show north, east and vertical displacements in meters (top to bottom). (A) Original GPS data for continuous GPS stations RGBY, DUMM, RVBM, RBED, and AC17 with outliers >3σ removed. Data from 2009.4 (May 26th, 2009) onwards (shown as gray dots) was used to estimate background linear trend and seasonal variations (shown in black for this period). These models were extrapolated into the past (shown in gray) to re-move linear and seasonal trends while preserving the volcanic signal. DUMM has no seasonal model removed due to its short time series. Arrows in east and north panel indicate estimated onset of precursory deformation at AC17. (B) Detrended data, stations are ordered in the same way as in the left panel. Black line shows smoothed time series created using a moving average with window size of 20 data points. Smoothing starts when stations are continuous. The dark gray box in the background marks the explosive period from March 22 to April 05, 2009. The lighter gray box marks the effusive period from April 05 to July 01, 2009 (Bull and Buurman, this volume). Dashed line for AC17 shows the post eruption average and illuminates pre-eruptive inflation and that the co-eruptive offset is overall larger than the pre-eruptive average in the horizontal field. Arrows in east and north panel indicate estimated onset of precursory deformation at AC17.

continuous deployments were recovered by AVO during times of relative quiescence of the volcano. The limited GPS real-time monitoring capability was completely eliminated when the RGBY antenna was hit by volcanic lightning. The lighting strike occurred within an hour of the last data download at about 10:00:00 UTC on March 23, 2009. Hence, it likely originated from the plume of event 04 (9:39 UTC) (Table 1 in Bull and Buurman, this volume).

RGBY shows inexplicable seasonal behavior similar to a sawtooth function (Fig. 2), which may result either from site specific freezing extension of water in cracks of the bedrock, or loading deformation due to its location close to a cliff near a Double Glacier outlet glacier (Fig. 1, left). The setting close to a cliff could lead to amplification of horizontal motion induced by seasonal loading of the glacier. However, first order attempts to remove such a contribution by modeling snow load effects on the position of the tip of a very long antenna pole (an approximation for the cliff) failed. To mitigate any site specific effects, the new GPS site RDJH was installed on August 20, 2010; the new monument, however, shows similar seasonal motion. We therefore report displacements at RGBY in figures and tables for completeness, but we ignore these values in analyses.

2.2. Static GPS data processing

We use the GIPSY-OASIS II software (Gregorius, 1996) developed at NASA's Jet Propulsion Laboratory (JPL) to compute Precise Point Positioning solutions (Zumberge et al., 1997) for the GPS data and then generate a time series of daily positions (Fig. 2A). We use the JPL reprocessed satellite orbit and clock products. Details on parameter estimation are given in Freymueller et al. (2008) and Freymueller and Kaufman (2010). Our processing strategy follows the general outline in Freymueller et al. (2008). Differences are that we use the IGS05 absolute antenna phase center models, GMF troposphere mapping function, and we apply ocean tidal loading based on the ocean tide model TPXO.7 computed with respect to the center of mass of the Earth system (Fu et al., 2012). We also transform site positions into the International Terrestrial Reference Frame (ITRF) 2008.

To eliminate effects of non-volcanic deformation we subtract the solutions of local reference stations from our network. We use this approach rather than a regional tectonic model because the tectonic motion in this region is complex and time-dependent, and published models leave unacceptable residual errors (Suito and Freymueller, 2009). The specific reference site varies depending on data availability during the investigated time span, but we use one of the continuous PBO stations whenever possible. We attempted using the PBO station AC59, about 100 km to the SW of Redoubt, as a reference station, because the closest continuous GPS station on the western side of Cook Inlet, AC17, shows deformation of volcanic origin during the studied period (Fig. 2). However, seasonal signals due to snow loading are different at AC59 compared to the Redoubt network, so we can use AC59 as reference station only over short time intervals such as the explosive phase (see Section 3), or over yearly intervals when surface loads are comparable. All models are computed relative to the appropriate reference site, so the choice of reference site mainly affects display of the data.

Displacements at the stations are estimated for time intervals by first calculating velocities from daily solutions, and using these to compute displacements over the investigated time periods (Table 2,

Table 2
Displacement table: Shows displacement values and uncertainties for each station in ENU direction for each of the periods described in the text.

Phase	Inter-eruptive			Pre-eruptive			Explosive		
Time	06/2001–08/2008 (wrt POLL)			08/2008–03/2009 (wrt AC17)			03/2009–04/2009 (wrt AC59)		
# solutions	17			46			14		
Site	E	N	U (cm)	E	N	U	E	N	U
AC17	–	–	–	0.00 ± 0.0	0.00 ± 0.0	0.00 ± 0.0	−0.64 ± 0.3	−0.85 ± 0.2	−0.23 ± 0.5
CRSC	0.19 ± 0.6	0.65 ± 0.4	−0.84 ± 1.3	–	–	–	–	–	–
DUMM	–	–	–	0.32 ± 0.3	0.94 ± 0.2	0.18 ± 0.6	−1.12 ± 0.3	−2.12 ± 0.2	−1.83 ± 0.6
NUNA	0.50 ± 0.6	1.05 ± 0.4	1.09 ± 1.2	–	–	–	–	–	–
POLL	0.00 ± 0.0	0.00 ± 0.0	0.00 ± 0.0	–	–	–	–	–	–
QRRY	0.19 ± 0.6	1.37 ± 0.4	−0.63 ± 1.4	–	–	–	–	–	–
RBED	0.41 ± 0.6	0.46 ± 0.4	−0.61 ± 1.2	0.02 ± 0.3	−0.97 ± 0.2	−0.46 ± 0.6	−0.18 ± 0.3	1.05 ± 0.2	−2.51 ± 0.5
RFFL	0.04 ± 0.5	0.06 ± 0.4	−0.58 ± 1.2	–	–	–	–	–	–
RGBY	−0.66 ± 0.6	0.11 ± 0.4	−1.41 ± 1.3	1.57 ± 0.2	1.91 ± 0.2	−1.14 ± 0.5	–	–	–
RNE	0.14 ± 0.6	0.67 ± 0.4	−1.20 ± 1.2	–	–	–	–	–	–
RTON	1.16 ± 0.5	0.71 ± 0.4	0.31 ± 1.2	–	–	–	–	–	–
RSUM	−0.04 ± 0.6	0.36 ± 0.4	−2.22 ± 1.2	–	–	–	–	–	–
RVBM	–	–	–	−1.25 ± 0.2	0.06 ± 0.2	0.81 ± 0.5	1.43 ± 0.3	0.07 ± 0.2	−2.43 ± 0.5
RVID	0.61 ± 0.6	0.49 ± 0.5	0.05 ± 1.4	–	–	–	–	–	–

Phase	Effusive			Full eruption			Post eruptive		
Time	04/2009–06/2009 (wrt AC59)			08/2008–06/2009 (wrt AC59)			06/2009–09/2011 (wrt AC17)		
# solutions	56			10			851		
AC17	−0.30 ± 0.1	−0.04 ± 0.1	−0.04 ± 0.3	−0.43 ± 0.2	−0.75 ± 0.1	−0.24 ± 0.4	0.00 ± 0.0	0.00 ± 0.0	0.00 ± 0.0
CRSC	–	–	–	1.70 ± 0.3	0.64 ± 0.2	−2.60 ± 0.6	–	–	–
DUMM	−0.66 ± 0.2	−0.30 ± 0.1	−1.31 ± 0.3	−0.43 ± 0.3	−1.44 ± 0.2	−3.04 ± 0.5	−0.16 ± 0.2	0.64 ± 0.1	−0.49 ± 0.4
NUNA	–	–	–	−0.46 ± 0.3	−1.03 ± 0.2	−2.23 ± 0.6	–	–	–
POLL	–	–	–	0.06 ± 0.3	0.87 ± 0.2	−1.64 ± 0.6	–	–	–
QRRY	–	–	–	0.15 ± 0.3	0.07 ± 0.2	0.46 ± 0.7	0.27 ± 0.4	−0.26 ± 0.3	−2.10 ± 0.9
RBED	−0.18 ± 0.2	0.65 ± 0.1	−0.80 ± 0.3	0.09 ± 0.3	0.47 ± 0.2	−3.35 ± 0.5	0.05 ± 0.1	−0.28 ± 0.1	1.08 ± 0.2
RFFL	–	–	–	−0.14 ± 0.3	0.97 ± 0.2	−2.35 ± 0.6	–	–	–
RGBY	−0.26 ± 0.2	−0.82 ± 0.1	1.14 ± 0.4	2.14 ± 0.2	−1.08 ± 0.2	−2.78 ± 0.5	0.24 ± 0.1	0.91 ± 0.1	0.10 ± 0.2
RNE	–	–	–	0.07 ± 0.3	−1.60 ± 0.2	−2.16 ± 0.5	–	–	–
RTON	–	–	–	−2.07 ± 0.2	−0.67 ± 0.2	−2.74 ± 0.5	–	–	–
RSUM	–	–	–	0.24 ± 0.3	−0.56 ± 0.2	1.26 ± 0.5	–	–	–
RVBM	0.38 ± 0.1	0.25 ± 0.1	−0.46 ± 0.3	0.83 ± 0.2	0.62 ± 0.2	−2.24 ± 0.5	0.11 ± 0.1	−0.07 ± 0.1	0.49 ± 0.3
RVID	–	–	–	–	–	–	–	–	–
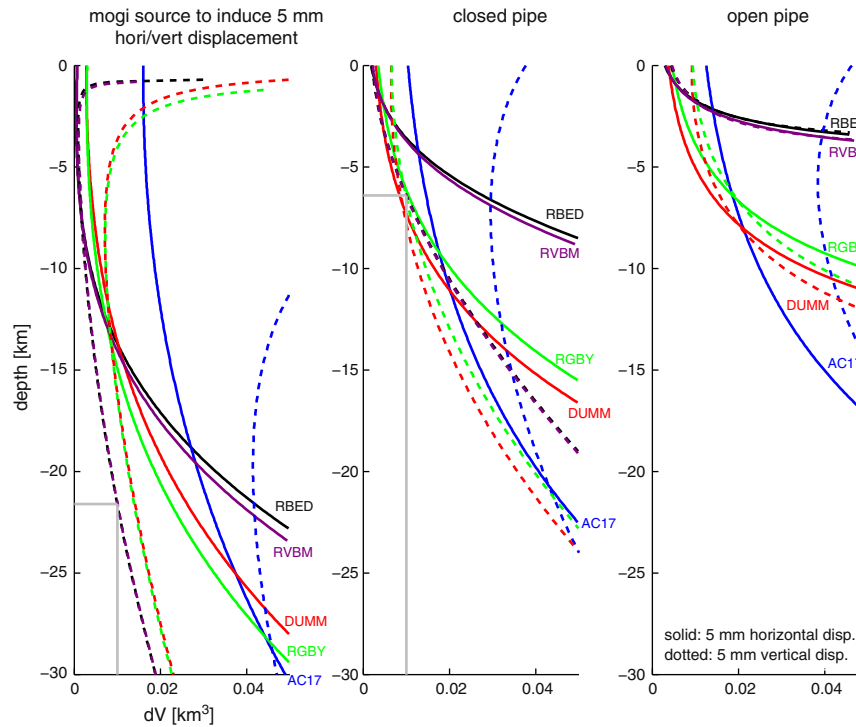
Fig. 3. Network sensitivity for Redoubt GPS stations testing Mogi source, closed pipe, and open pipe with a source assumed centered underneath Redoubt's last dome from 2009 (Diefenbach et al., this volume). Colors refer to different stations; station names label respective lines. Solid and dotted lines represent horizontal and vertical 5 mm iso-displacement lines, respectively. A source that plots to the right of the line for a given station would produce > 5 mm displacement at that station. Gray boxes indicate how to find maximum depth for a given volume change (and vice versa) and which stations will show deformation. (For interpretation of the references to color in this figure legend, the reader is referred to the web version of this article.)

exact date ranges given in Section 4). The uncertainties of the displacements are the scaled uncertainties of the velocities, which are based on a white noise model only. This could be too optimistic for longer time series of continuous stations as these also include colored noise. However, except for the interval from August 2008 to June 2009, the other periods are at most 56 days long and rescaling the uncertainties is not a problem. For the 9 month long period, we used only the days of the GPS campaigns at either end of the observation period for both campaign and continuous stations, which avoids this problem and also avoids the need to model the full time dependence of the continuous time series. Because of this approach, the uncertainties for the continuous GPS sites in Table 2 (column "Full Eruption") are roughly the same as for campaign sites.

To highlight the volcanic signals in the time series, we estimated and removed long term linear and seasonal models for the PBO and temporary continuous GPS stations. We first eliminated outliers using a 3σ test and then estimated trends based on post-eruption data from decimal year 2009.4 (May 26, 2009) to the present, shown as gray dots in Fig. 2A. The estimated trends were extrapolated into the past and removed from the time series, which should preserve volcanic signals. For the seasonal signal we estimated annual and semi-annual cosine and sine functions; only at RGBY we allowed an additional saw-tooth function to be estimated (Fig. 2). This highlights the different phases of deformation in relation to the eruptive phases.

2.3. Kinematic GPS data processing and phase residuals

We estimate kinematic solutions for the time period of the explosive phase to determine subdaily position estimates. In the kinematic solutions, we have to assume that all stations are in motion with respect to a fixed base station. To estimate kinematic station trajectories we use the software `track`, which is part of the GAMIT-GLOBK GPS processing package (Herring et al., 2010). Here, we use IGS satellite orbits (Dow et al., 2009) and estimate tropospheric delay based on the global pressure/temperature and global mapping functions (Boehm et al., 2006, 2007; Kouba, 2009) implemented in `track`. As our focus for the kinematic solutions is on short term displacements in relation to individual events during the explosive period, we assume that AC17 remains stable during these events and use it as base station. This gives baselines of generally less than 40 km between rover and base station, and allows us to assume similar travel paths for the satellite signals arriving at the stations.

During kinematic processing we found systematic positioning outliers/spikes (described in Section 5) which we try to explain using satellite phase residual values (RMS) as reported by the GIPSY software using a kinematic network processing mode. To plot the phase residuals, we use the `cf2sky` code by Hilla (2004); `cf2sky` visualizes `teqc` (Estey and Meertens, 1999) plot files along a satellite's trajectory in a skyplot. We modified `cf2sky` to run on a Linux platform and translated GIPSY postfit data into UNAVCO COMPACT format readable by `cf2sky`.

3. Modeling

3.1. Volcanic source models

Because of the limited data available and the lack of previous geodetic studies for Redoubt, we have to make several assumptions to simplify the system. Assuming the magma source is embedded in an elastic, isotropic and homogeneous half space is without doubt the most drastic simplification (Masterlark, 2007). Elasticity is justified by the short timescale of our investigation. Isotropy is justified by the symmetry seen in the data (see Section 4). Homogeneity is the least likely assumption, but no adequate 3D model of elastic moduli exists. Consequently, these assumptions allow us to use simple

analytical models instead of heavily underdetermined systems of equations or poorly constrained finite element models.

As the data shows a radially symmetric deformation pattern (see Section 4), we limit our modeling efforts to radially symmetric pressure sources: a pressure point source considering topography (Mogi model) (Anderson, 1936; Yamakawa, 1955; Mogi, 1958), and prolate spheroids in a flat half-space (reference surface is shifted to sea level). Of the prolate spheroids, we test two types: a degenerate version with a semimajor axis much larger than the semiminor axes (from here on referred to as open/closed conduit) (Bonaccorso and Davis, 1999; Segall, 2010), and a general formulation that does not assume a certain axes aspect ratio (Yang et al., 1988; Newman et al., 2006; Battaglia et al., 2012), which we keep vertical and radially symmetric, though.

The Mogi model has 4 parameters: horizontal location, depth and source strength of the pressure point source. A conversion from source strength to volume change is given, for example, by Sigmundsson (2006, Equation 5.11) assuming incompressible magma. The conduit and spheroid models share these parameters, but replace the single depth with the upper and lower ends of the vertically elongated source. The general formulation of the prolate spheroid requires solving for the length of the semiminor axis, which results in 6 free parameters for this model.

The source strength, C, of a conduit is given in terms of pressure change, ΔP, conduit radius, a, and shear modulus, G (e.g., Segall, 2010).

$$C = \frac{a^2 \Delta P}{4G} \tag{1}$$

To express the source strength in terms of volume change, which is what we are ultimately interested in, we first solve the fluid pressure formula in terms of ΔP:

$$\Delta P = K \frac{\Delta V}{V} \tag{2}$$

where K is the bulk modulus, and V is volume.

The volume of a spheroid is $V = 4/3 \pi a^2 (c_2 - c_1)$ where c_1 and c_2 are upper and lower ends, respectively. If we express the bulk modulus in terms of Poisson ratio ν and shear modulus G, we get the source strength in Eq. (1) in terms of volume change as:

$$C = \frac{1+\nu}{2(1-2\nu)} \frac{\Delta V}{4\pi(c_2 - c_1)}. \tag{3}$$

In addition to the single source cases, we also tested cases with 2 sources using combinations of two Mogi sources as well as a shallow conduit and a deep Mogi source. However, the improvement in fit to the data for these models was never significant based on an F-Test, so we do not report results of these tests.

To find a source that fits the data, we implement a two-stage grid search over the spatial domain; although computationally more costly than other non-linear inversion methods, this is straightforward to implement and practical considering the sparse data.

We start on a coarse grid with an area of 10 km × 10 km centered on the location of the final dome of the 2009 eruption (Diefenbach et al., this volume). On this grid we search for sources between 1 and 40 km depth. The grid node spacing for both, horizontal and depth search is 1 km. All best fitting source models were located within a 5 km radius from the last dome, so we densified the search grid over the center area of 5 km × 5 km. We search again for sources between 1 and 40 km depth with a grid node spacing of 250 m in every direction. We estimate the volume change, ΔV, over the respective time period using least squares inversions for each set of

geometric parameters. For conduits and spheroids we also assume that the lower end is at least one grid cell below the upper end.

The best source parameter combinations are found by minimizing χ^2 (Press et al., 2007), which compares measured and modeled displacements and provides a quantitative measure of misfit for each set of parameters. We select the best fitting source within the search space corresponding to a physically reasonable local minimum of χ^2. Confidence intervals for each parameter are picked based on $\Delta\chi^2$ values assuming one degree of freedom projected on the axis of the respective free parameter (Press et al., 2007). We give confidence intervals at the 95% level.

To reduce computational cost, we only search for a general prolate spheroid when a conduit model provides a better fit than the Mogi source and the pressure change in the conduit would be greater than lithostatic stress, as conduit models in that case would be unphysical. We search over semimajor axis lengths from 1 km to 7 km in 250 m increments and over semiminor axis lengths from 0.1 km to 1 km in 25 m increments assuming a crustal shear modulus of 26.6 GPa (Turcotte and Schubert, 2002).

3.2. Network sensitivity analysis

A question seldomly addressed when interpreting geodetic signals at active volcanoes is which signals a network cannot resolve, i.e., what is the smallest source at a given depth we can possibly infer from the data? This has important implications on the interpretations of the signals actually resolved in the data, the plumbing system of a volcano we infer from these data, and how geodetic observations can be incorporated into observations of other disciplines.

Let us assume we can detect position changes greater than 5 mm in the data, which is just above GPS noise. We apply the Mogi model (topography corrected, see Yamakawa (1955)), the closed and open conduit model and try to find the smallest, shallowest source between 0 and 30 km depths (100 m steps) that induces detectable displacements (>5 mm). For the purpose of this analysis the source is assumed to be centered under the location of the final dome of Redoubt's 2009 eruption (Diefenbach et al., this volume). The pipes are defined as 15 km long since the lower end has only small effects on the deformation field. Fig. 3 shows the results: each line indicates the depth–volume change dependence for each station that would produce significant displacements. Solid and dotted lines represent horizontal and vertical 5 mm iso-displacement lines, respectively. The colors are the same for each station in all three panels as indicated in the legend. The gray lines in the panels for the Mogi source and the closed conduit assist in interpreting this plot. For the Mogi source we see that a volume change of 0.01 km³ at 21.6 km will induce 5 mm of vertical displacement at RBED and RVBM. No displacements above the 5 mm threshold will be recorded at any of the other stations for this source. Similarly, we can see that a volume change of 0.04 km³ in a Mogi source at 15 km will induce displacements above the threshold in both components at all sites except AC17 where it only affects the horizontal component. For a closed conduit we can see that the network will not show displacements induced by volume changes smaller than 0.01 km³ at depths greater than 7.5 km. An open conduit will be detected only if it is shallower than 10 km with volume changes greater than 0.02 km³.

4. Long term displacements: estimating volcanic source parameters

The first GPS campaign measurements at Redoubt were done in January and June of 1991; the latter producing most of the data (Fig. 1). Half of the receivers used in June 1991 produced questionable L2 phase data, so several sites had to be excluded. The uncertainties associated with such early GPS data are much larger than for current measurements. This complicates precise estimation of displacements to infer volcanic deformation. However, the bigger issue with these
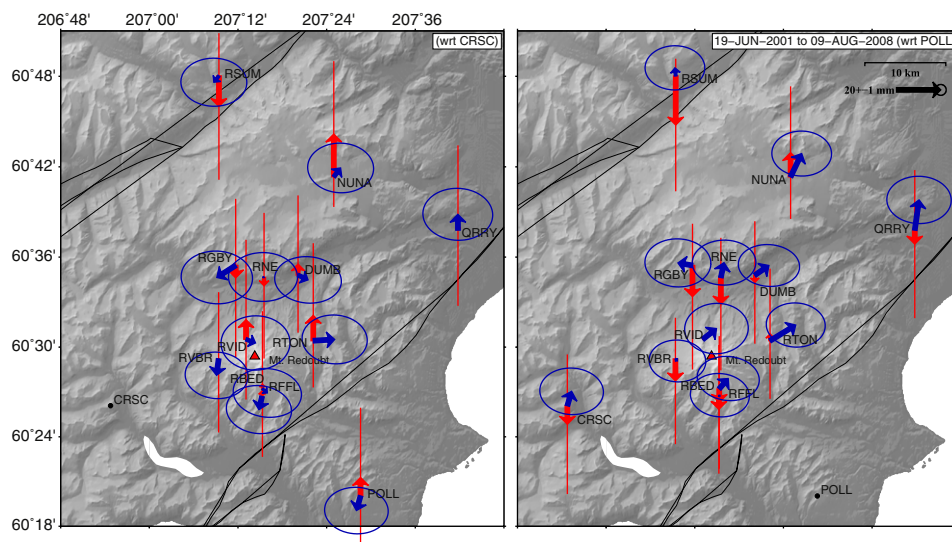
Fig. 4. Displacements from 2001 to 2008 (inter-eruptive period) with respect to CRSC (left) and POLL (right). Blue vectors are horizontal displacements, red vectors are vertical displacements. Arrows are tipped with 95% confidence ellipses/lines. Numerical values for displacements (wrt POLL) are given in Table 2. Neither referencing the displacements to CRSC (left) nor to POLL (right) reveals a pattern consistent with deformation at Redoubt. (For interpretation of the references to color in this figure legend, the reader is referred to the web version of this article.)

data is that only very few stations defined the global reference frame at that time. These stations also differ from those defining the current ITRF. It is possible to align the earlier measurements to the current reference frame by applying station ties between old and current stations realizing the reference frame. However, at the time of this writing, this process could not be completed to sufficient precision. Analysis of baselines between stations shows no evidence for volcanic deformation larger than the noise level, so these data are not discussed further.

Based on the intervals of GPS data collection as well as activity of the volcano, we look at displacements over various periods of time. Bull and Buurman (this volume) separated the eruption into distinct phases based on changes in activity. However, we cannot follow their dates exactly due to the times at which the GPS sites were reoccupied (Fig. 1). For example, we define the end of the effusive phase as the time of a survey in June 2009 while Bull and Buurman (this volume) define July 2009 as the end. We also see no deformation associated with the explosive event on March 15, which is why our precursory phase extends to March 22, 2009, after which juvenile material was extruded. The displacement values for the individual phases of the eruption as displayed in Figs. 5–8 are compiled in Table 2.

4.1. Inter-eruptive period (06/2001–08/2008)

We use 17 daily positioning solutions to constrain displacements with respect to CRSC and POLL (Fig. 4) from June 19, 2001 to August 09, 2008. Neither AC59 nor AC17 was operational in 2001 and they could therefore not be used as reference stations. The maximum displacements over a period of 7 years remain below 15 mm in the horizontal and vertical with uncertainties of 4–6 mm and 12–14 mm, respectively. The spatial signature of the signal seems largely non-volcanic with local effects at POLL likely due to tectonic deformation. NUNA shows uplift, likely due to melting of the Double Glacier ice cap.

4.2. Precursory phase (08/2008–03/2009)

As the first explosion containing juvenile material was reported on March 23, 2009 (Bull et al., 2012; Bull and Buurman, this volume), we

consider the time between the campaign in 2008 and this event the precursory phase. At this time, only 4 stations of the Redoubt network were operating due to their conversion to temporary continuous sites. However, in addition to this, the continuously recording station AC17 gives a good record of far field deformation indicating the
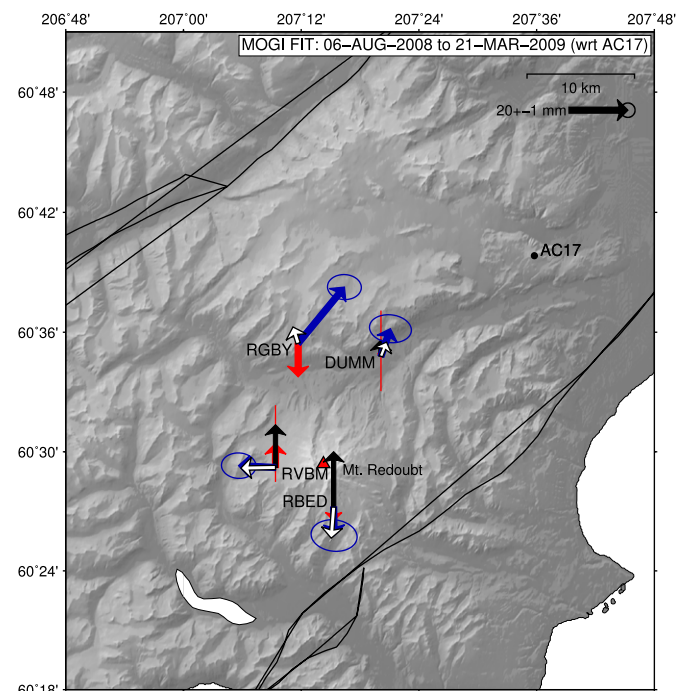

Fig. 5. Displacements during pre-eruptive period from August 2008 to March 2009 with respect to AC17 (blue: horizontal, red: vertical) and displacements induced by a preliminary model (white: horizontal, black: vertical) inferred from horizontal displacements only. Data arrows are tipped with 95% confidence ellipses/lines. Preliminary model predictions assume a Mogi source at depth $d = 21.75$ km with volume change $dV = 0.1018$ km^3 (see column "preliminary precursory" in Table 3). The red triangle marks Mt. Redoubt. (For interpretation of the references to color in this figure legend, the reader is referred to the web version of this article.)
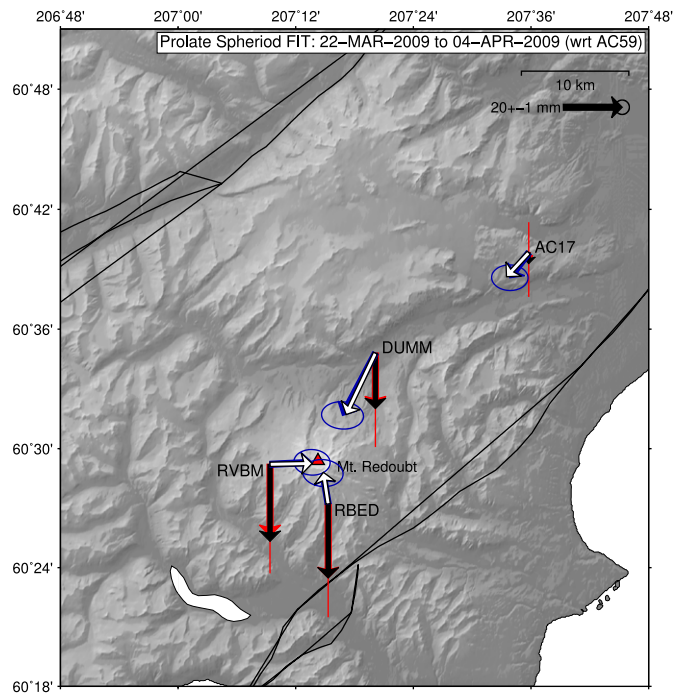
Fig. 6. Displacements and model fit during explosive period from 22 March to 04 April with respect to AC59. Same symbols as in Fig. 5. Both, vertical and horizontal data are fit well by the model. Vectors from all stations point straight at position of last dome (red triangle). (For interpretation of the references to color in this figure legend, the reader is referred to the web version of this article.)
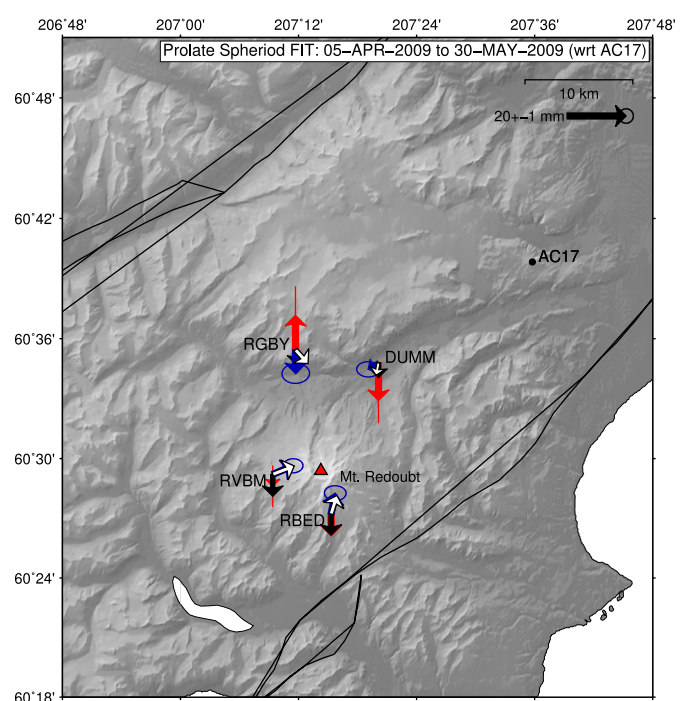
Fig. 7. Displacements (blue: horizontal, red: vertical) and model fit (white: horizontal, black: vertical) for effusive period from 05 April to 30 May with respect to AC17. The model fit assumes the same prolate spheroid geometry as the explosive phase with volume change $dV = -0.0167$ km^3 (see column "effusive" in Table 3) and is based on the fit to displacements at RBED and RVBM only. Data arrows are tipped with 95% confidence ellipses/lines. The red triangle marks Mt. Redoubt. (For interpretation of the references to color in this figure legend, the reader is referred to the web version of this article.)

reversal of the subtle pre-eruptive deformation trend with the onset of explosive activity (see Fig. 2).

The time series of AC17 (Fig. 2) gives the most insight into the timing of deformation during the precursory phase. The horizontal time series shows a clear deviation from the long term trend during this phase when compared to the trend of the post-eruption data. The onset of this change in motion is hard to pin-point to a specific date, but with some confidence we estimate it to be approximately May 2008. The north component shows this change in trend more clearly than the east component; the combined horizontal motion is toward the NE. Generally speaking, this motion is consistent with a deep intrusion under Redoubt.

The vertical component at AC17 contains interesting, but mostly non-volcanic motion. Given the large distance of about 28 km from the volcano most analytical source models suggest no or very little vertical deformation at the station. Fig. 2, however, shows small relative subsidence from the beginning of 2008 through the end of the effusive period in 2009. The mean of the detrended vertical data for

AC17 (dashed line in Fig. 2) highlights this observation. Rather than a volcanic signal, it is likely loading due to residual snow from an unusually cold summer in 2008 (Anthony Arendt, pers. comm., unpublished GRACE data). Grapenthin et al. (2006, 2010) and Pinel et al. (2007) show that surface loading hardly affects the horizontal signal when the vertical signal is this small, which assures us that the horizontal signal is volcanic. We do not have enough data to model and remove the snow effect and hence do not use vertical motion at AC17 to model volcanic effects.

We attempted to evaluate the displacements at AC17, DUMM, RBED, and RVBM during the precursory phase with respect to AC59. However, a difference in snow loading obscures the small volcanic signal in horizontal displacements at DUMM, RBED, and RVBM. We remove this by displaying these data with respect to AC17 (Fig. 5), which results in vectors pointing radially away from the volcano

Table 3
Best fitting models. Depth values in parenthesis are actual model results not topography corrected as for the spheroids the average elevation had to be removed to move the reference surface to sea level and give depths below sea level. Confidence intervals (superscripts and subscripts) are given at the 95% level. Bold font highlights final models.

	Preliminary precursory		Final precursory		Explosive		Effusive	
Stations	DUMM, RBED, RVBM		AC17, CRSC, NUNA, RBED, RFFL RNE, RSUM, RTON, RVBM		AC17, DUMM, RBED, RVBM		RBED, RVBM	
# observables	6 (horizontal only)		18 (horizontal only)		12 (horizontal + vertical)		6 (horizontal + vertical)	
Average elevation (m)	1145.01		1202.67		1079.40		1601.70	
Source geometry	Closed conduit	Mogi	**Mogi**	Prolate spheroid	**Prolate spheroid**	Mogi	**Prolate spheroid**	Mogi
Centroid depth (km)	10.61 (11.75)	21.75	**13.50** $_{17.33}^{10.17}$	See explosive	**9.17** $_{15.17}^{6.92}$ (10.25)	15.25	See explosive	8.75
Semimajor (km)	12.00	–	–	See explosive	**4.50** $_{>10.00}^{1.25}$	–	See explosive	–
Semiminor (km)	0.025	–	–	See explosive	**0.475** $_{>4.00}^{0.3}$	–	See explosive	–
ΔV (km^3)	0.0309	0.1018	**0.0194** $_{0.0340}^{0.0092}$	**0.0278** $_{0.0341}^{0.0214}$	-(**0.05** $_{>0.1}^{0.028}$)	−0.0303	-(**0.0167** $_{0.0228}^{0.0106}$)	−0.0034
dx (km)	−1.75	−3.25	**0.00**	See explosive	**0.50**	1.00	See explosive	1.75
dy (km)	−2.75	−4.00	**−1.25**	See explosive	**0.00**	0.25	See explosive	1.75
χ^2	0.1005	1.1426	14.2667	18.54055	0.2450	11.0137	0.7468	0.1470

consistent with influx of material underneath. Compared to the total deformation from 2001 to 2008, these displacements are significantly larger over the short period of about half a year.

Although the horizontal data suggests a volcanic source, vertical displacements are small or zero (Fig. 5). This is likely due to seasonal loading, which is more prominent at higher elevations. Given the topography and assuming a volcanic source under the volcano, this counteracts an inflationary vertical signal. However, as mentioned above loading does not affect horizontal motion as much as volcanic sources, which gives us confidence in the volcanic origin of this signal.

As a result of these seasonal loading effects, searching for a source using the vertical displacements (Fig. 5) could result in a biased model. Therefore we attempt to find a source using only the horizontal displacements at DUMM, RVBM, and RBED relative to AC17. While the best fitting model for these horizontal displacements is a closed conduit (Fig. 3), an F-Test suggests that the smaller χ^2 value for this source does not justify the additional free parameter above that of the Mogi model. Hence, we consider the Mogi source at 21.75 km bsl with a volume increase of 0.1018 km^3 about 3.25 km to the W and 4.00 km to the S of the last dome to be the best model (Fig. 5). We will reassess this source model at a later point using data that span all phases, at this point we will also derive confidence intervals for the parameters.

4.3. Explosive phase (03/2009–04/2009)

The explosive phase spans only 14 days, which renders tectonic and seasonal effects negligible, and we can use AC59 as a reference site. From the onset of the first explosion on March 23, 2009, to the last explosion on April 4, 2009, we see clear displacements at AC17, DUMM, RVBM, and RBED (Figs. 2 and 6). All sites move down and toward the vent, and give the largest signal of the sequence with up to 2 cm horizontal and 2.5 cm vertical motion (see Table 2).

We use the displacements at these 4 sites to estimate the source parameters. A closed conduit model fits better than a Mogi model. However, the inferred volume change of $\Delta V = -0.0275$ km^3 for this model suggests a conduit radius of about 38 m and a pressure change of 44 GPa, several orders of magnitude higher than lithostatic stress at these depths (0.26–0.29 GPa, (Turcotte and Schubert, 2002)). This stress regime is unphysical for a conduit, i.e. a dike would form to reduce such high pressures which a conduit could not withstand. Since the deformation pattern does not support the formation of a dike, we reject this model and search for a prolate spheroid with an unknown semimajor–semiminor-aspect ratio using an implementation provided by Battaglia et al. (2012). We limit the maximum pressure change to the lithostatic stress (when not limiting the pressure change to lithostatic stress, the preferred source is a conduit with approx. 35 m radius, similar to the conduit model presented above). The best fitting source is offset by 0.5 km to the East from the last dome. Its centroid is at 9.17 $^{6.92}_{15.17}$ km bsl, the semimajor axis is 4.5 $^{1.25}_{>10}$ km long and the radius is 0.475 $^{0.30}_{>4.00}$ km (superscripts and subscripts refer to upper and lower ends of confidence intervals at the 95% level). The inferred volume change is $-(0.05\ ^{0.028}_{>0.1})$ km^3. Note that the unconstrained values in the confidence intervals indicate that the bottom end of the source is not well constrained by the data. The model fit is given in Table 3 and shown in Fig. 6; an F-Test confirms that the improvement in fit warrants the use of two additional free parameters compared to the Mogi model.

4.4. Effusive phase (04/2009–06/2009)

After April 4, 2009, explosive activity ceased and the final, persisting dome was built. As Fig. 2 indicates, AC17 is moving at pre-eruptive rates after the explosive phase. Hence, we assume no volcanic signal at this station and give the displacements relative to this site (Fig. 7). Small displacements measured at RVBM and RBED

likely indicate the evacuation of small amounts of material from shallow to mid-crustal depths. However, interpretation of these displacements is difficult, as the dome emplacement creates a loading signal at the surface which in turn is also obscured by uplift due to seasonal melt as indicated by displacements at RGBY. DUMM shows the largest subsidence signal which is likely related to significant lahar deposits in the Drift River Valley (Waythomas et al., this volume). This is supported by slight up-valley horizontal motion toward the thicker deposits of the lahars.

Due to the site specific motion at DUMM and RGBY we use only RVBM, and RBED to infer source parameters. The best fitting source is a Mogi source at a depth of $d = 8.75\ ^{3.50}_{18.00}$ km bsl with a volume change of $\Delta V = -(0.0034\ ^{0.0012}_{0.0148})$ km^3. It is horizontally offset to the North and to the East respectively by 1.75 km (Table 3). The conduit model gives almost as good a fit, but the upper and lower ends are basically at the same depth, suggesting the extra parameter is not warranted by the data.

Since the depth of the Mogi source coincides with the centroid of the prolate spheroid inferred for the explosive phase, we test whether using the explosive source with a different volume change provides an acceptable fit. Indeed, the explosive source with a volume change of $\Delta V = -(0.0167\ ^{0.0106}_{0.0228})$ km^3 provides almost as good a fit ($\chi^2 = 0.7468$) as the Mogi source ($\chi^2 = 0.1470$). An F-Test shows the slight difference in χ^2 does not justify the necessary 3 additional free parameters for the Mogi model. Therefore, we favor the simple interpretation that activity continued from the source of the explosive phase (Table 3, Fig. 7), given the very small amount of data for this phase.

4.5. Full period of unrest (08/2008–06/2009)

As the whole network was remeasured in a campaign in June 2009, we show the displacements between August 06, 2008, and June 10, 2009 with respect to AC59 (Fig. 8A). The figure shows a clear volcanic signal, which suggests that the necessity to use AC17 as reference station for the 2–6 months periods investigated above was mainly due to seasonal effects. This time period, however, spans most of the intrusion of material as well as the explosive and effusive activities; the displacements, in turn, reflect the superposition of motion resolved in the individual phases above. This gives a very undifferentiated view in terms of temporal evolution of the system, but clearly shows that the motion at all stations is consistent with a net evacuation of material. To confirm the robustness of our source estimates, we compare the sum of individually modeled displacements for each phase (precursory phase: Mogi source at 21.75 km, explosive and effusive phases: prolate spheroid at 10.25 km with respective volume changes listed in Table 3) to the larger dataset with respect to AC59 (Fig. 8A).

The full model significantly overestimates the vertical displacements at all sites, predicting uplift while most sites show subsidence. The horizontal displacements are overestimated in magnitude for some and underestimated for others; the azimuths of horizontal displacements are significantly off at many sites. Generally, we can say that the combined model does not predict the measured displacements well. We believe this is mainly due to the poor constraints we have on the precursory model. To extend our data set for that period we predict the displacements at all sites using the source models for the explosive and effusive periods (Table 3, Fig. 8B). Removing these predicted displacements from the data, we get residuals that contain the precursory signal plus any other non-volcanic signals (Fig. 8C,E). While the vertical residuals in Fig. 8C,E are likely affected by non-volcanic signals, the horizontal components at most stations indicate an inflation signal. We use almost all stations to invert this extended horizontal displacement data set for a precursory source. In addition to the routine exclusion of RGBY we also exclude the stations QRRY, POLL and DUMM from our source estimations. Horizontal

motion at QRRY differs significantly in magnitude from the nearby AC17. POLL shows a different direction in the horizontal, likely because it is on the far side of the Bruin Bay Fault to the SE of Redoubt. DUMM is likely affected by a loading signal due to lahar deposits. We found that inversions that include DUMM result in a significant increase in model misfit and a preference for an unrealistically long conduit from 2.25 km to 19 km depth with a very small volume increase of just 0.0063 km^3.

The best fitting source using the remaining stations is a single Mogi source located at 13.50 $^{10.17}_{17.33}$ km depth, 1.25 km to the S of the last dome with a volume change of $\Delta V = 0.0194\ ^{0.0092}_{0.0340}$ km^3 (Fig. 9). The fit of this model to the data residuals is shown in Fig. 8C. Fig. 8D shows the fit of the sum of the models for explosive, effusive, and this corrected precursory model.

Physically this source represents an injection of material at the base of the prolate spheroid inferred from the explosive data. If we proceed in a similar manner to the effusive phase and reuse the explosive source geometry varying the volume change only, we get a best fit for $\Delta V = 0.0278\ ^{0.0214}_{0.0341}$ km^3. The fit of this model to the data residuals is shown in Fig. 8E. Fig. 8F shows the fit of the sum of the models for explosive, effusive, and this corrected precursory model.

The fits of both models are rather similar ($\chi^2_{\text{mogi}} = 14.75$, $\chi^2_{\text{ps}} = 18.54$) and not as good as for the other periods. An F-Test is not as conclusive as for the effusive phase to decide whether the slight improvement in fit of the Mogi model justifies the addition of three parameters ($F(3,14,0.05) = 3.3439 > 1.1958$). We therefore provide both models as possibilities — precursory inflation could have involved either the same source as the other phases, or only inflation at its lower depth limit.

4.6. Post eruption (06/2009–onward)

The time series with linear and seasonal trends removed (Fig. 2) clearly shows an absence of consistent volcanic deformation after June 2009. A small vertical offset at RBED is noted at the beginning of June 2009, likely unrelated to volcanic activity due to its rapid nature. DUMM does not show anything similar and RVBM was not operational at this time, so the origin of this signal remains unexplained.

5. Short term displacements: picking up plumes

We estimate kinematic trajectories to investigate subdaily motion for stations RVBM, DUMM, and RBED with respect to AC17. The sampling interval for most receivers during the 2009 Redoubt eruption was 30 s (AC17, RGBY sample at 15 s), which we use as the time resolution in the processing without any data decimation. Figs. 10–12 show the subdaily position time series from March 22 to April 05, 2009, for these three stations. Since the presented time series spans 15 days, they clearly resolve the long-term trend due to removal of material at depth, which we investigated above (see Section 3). Here, we did not attempt to remove multi-path effects (e.g., Larson et al., 2007) as we do not interpret any small amplitude features and the long time span allows us to discern whether the signals we interpret repeat approximately daily. A good example of multipath is the repeating signal in the vertical time series for RBED in Fig. 12.

Stations RVBM and DUMM experience significant spikes or outliers that correlate very well with the timing of explosions (shown in light gray in Figs. 10 and 11). Of the 28 explosive events determined through seismicity (Bull and Buurman, this volume, Table 1), 17 plumes reach higher than 12 km asl. 12 of these induce position

spikes at RVBM where we see no false-positives during the explosive phase. 3 plumes induce position spikes at DUMM; 1 of these is not seen at RVBM (March 28, 23:29 UTC, Event 17). At DUMM we see one false-positive indicated by arrow A in Fig. 11 and discussed below. The remaining 11 plumes reached altitudes below 8.5 km or the plume heights could not be determined.

As shown by Houlié et al. (2005a) for Miyakejima and Houlié et al. (2005b) for Mt. St. Helens, these changes in position may be due to path delay effects induced by ash plumes injected into the atmosphere during explosions. The presence of ash increases the travel time of signals from the satellite to the station. This inhomogeneous path delay is not modeled when tropospheric path delay effects are estimated during the GPS solution and it affects satellite–station-pairs that cross the vent or ash rich plume (Houlié et al., 2005a). In cases where base station and rover are on opposite sites of the vent, an apparent baseline lengthening occurs. The RVBM time series (Fig. 10) shows this very well as RVBM is consistently offset to the SW and up during these events. In addition to these spikes in position at RVBM, the associated RMS values (Fig. 10, lowest panel) reported by `track` show a spike, indicating a poor fit to the data at these times. As `track` does not report postfit phase residuals individually for each satellite, we refer to the values reported by GIPSY from kinematic network solutions that we have run in parallel (we do not show time series from these as artificial position offsets at day boundaries occur in the GIPSY solutions when using the JPL orbit and clock products).

Figs. 13 and 14 show phase RMS plotted along the satellite sky tracks for March 26 and April 04, 2009, respectively. These skyplots cover the times during which event 08 and 19 occurred (see Table 1 in Bull and Buurman, this volume). In the following we first explain signals related to these events and in Figs. 16 and 17 we cover a few anomalies where we do not see a plume related signal or see a very large non-plume induced effect. Details on how to read these figures are given in the caption of Fig. 13.

At almost 19 km asl, the plume of event 08 on March 26, 2009 (17:24 UTC), is one of the largest of the entire eruption (Bull and Buurman, this volume; Schneider and Hoblitt, this volume). Bull et al. (2012) show tephra iso-mass contours for this event extending to the S and SSE of the vent. The contours cross Cook Inlet and highest ash-fall was sampled up to the shore. Fig. 13 shows the phase residuals for satellites visible from 17:00 to 18:30 UTC. Both AC17 and RBED show small residuals at the time of event 08. They share a similar spike for PRN 21. RVBM on the other hand shows residuals distinctly different from those at AC17 at the time of the explosion (marked in red in Fig. 13). PRN 26 and 15 to the ENE, PRN 21 to the E and PRN 18 to the SE show large spikes coinciding with the explosion. At DUMM a residual for PRN 16 in the southern sky seems more pronounced than at the other stations. These observations are consistent with a plume indicated by the tephra dispersion map of Bull et al. (2012) and remote sensing observations of the plume (Webley et al., this volume). Given the narrow footprint of this plume and its direction combined with the satellite distribution only the clear lack of signal of PRN 22 at RBED seems surprising. We believe this can be explained by its low elevation above the horizon (30°) — the satellite may have been below the thick part of the plume.

On April 04, 2009, the plume went to the SE, and left a very narrow footprint (Bull et al., 2012). Fig. 14 shows that AC17 and RBED see about the same level in noise for all satellites with slightly higher amplitudes in phase RMS at RBED for PRN 3, 6, and 16 in the WNW sky. The general noise characteristic for these satellites can be

Fig. 8. Displacements relative to AC59 from August 2008 to June 2009 spanning the full eruption. Clearly, we see a net deflation, i.e., net loss of material. Each panel shows different forward models (black and white vectors). (A) Sum of displacements for the best fitting sources from preliminary precursor, explosive and effusive periods provides poor fit to the data. (B) Sum of displacements due to explosive and effusive sources only (prolate spheroid). The residuals, inferred to represent the precursory deformation are plotted as colored vectors in (C) and (E). (C) Fit of best Mogi model (black and white vectors, see Table 3) to residuals (colored vectors). (D) Sum of displacements for all source models using the source model derived from (C) as precursory source model. (E) Best fitting volume change of explosive source model (black and white vectors, see Table 3) to residuals (colored vectors). (F) Sum of displacements for all source models using the source model derived from (E) as precursory source model.
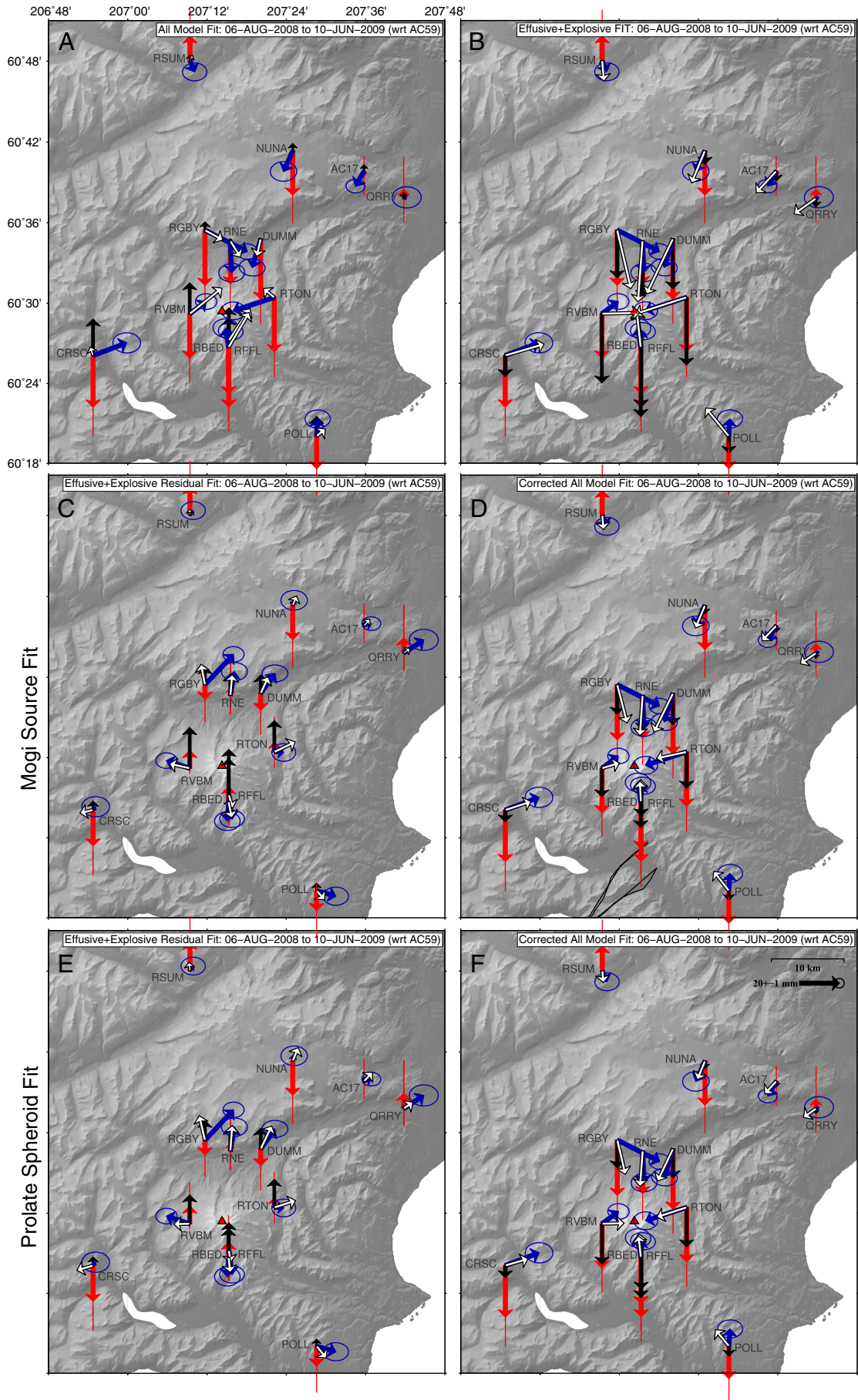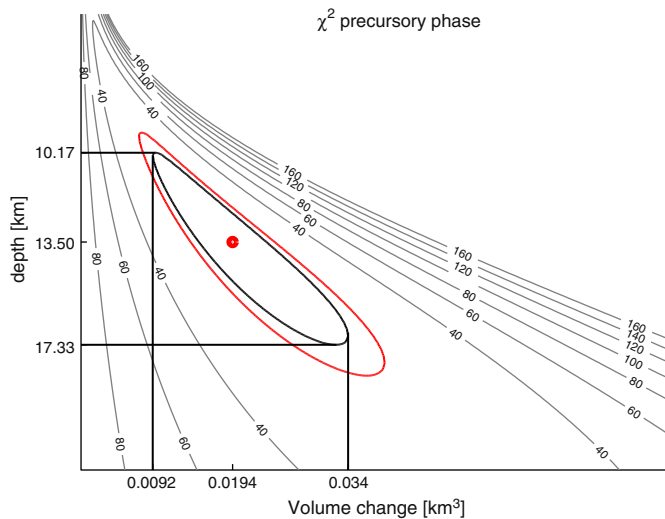
Fig. 9. χ^2 contour plot showing change of misfit depending on variation of the two parameters depth and volume change for the precursory phase derived from displacements for the full event. Red dot is best fitting model from the inversion. Ellipses show confidence intervals at 95% level derived from $\Delta\chi^2$; red ellipse for two free parameters; black ellipse assumes one free parameter at the 95% confidence level and is used to project confidence intervals on the axes (black lines; see Press et al. (2007)). (For interpretation of the references to color in this figure legend, the reader is referred to the web version of this article.)

explained by a ridge to the WNW above RBED, which makes this station more sensitive to low angle signals. At the time of Event 19, from 13:58 to about 15:00 UTC (see Table 1 in Bull and Buurman, this volume), most of the satellites are in the southerly sky or rather low to the WNW (PRN 16) and ENE (PRN 10). Both AC17 and RBED seem to have an undisturbed atmosphere between them and the satellites (compare to station positions in Fig. 1). RVBM and DUMM, which are to the W and ENE of the vent, however, show distinct phase residuals. At about 14:30 UTC PRN 10 shows a big spike in

phase RMS at RVBM while the residual for this satellite at DUMM is similar to AC17 and RBED. Smaller spikes at about the same time are visible to the WNW (PRN 16), SSE (PRN 30), and ESE (PRN 24, 29) at RVBM. The case is rather different for DUMM which shows the largest spikes for PRN 31, 21, and 30 from the SW to the SSE. While the residuals at DUMM seem consistent with disturbance by the plume, the directionality of the large spike at RVBM seems to correspond to the location of pyroclastic density current deposits (compare Fig. 4 in Bull and Buurman, this volume). If we remove the satellites from the processing when they experience plume-related path delays, we can reduce the number of outliers and reported RMS significantly (Fig. 15) which underlines the impact of the unmodeled disturbances of the atmosphere that increase the phase delay (Houlié et al., 2005a, 2005b).

Although we seem to pick up many plumes in the phase residuals at RVBM, a few, some of which reached significant altitudes, are 'missed.' In Fig. 16 we show the skyplots of DUMM and RVBM for March 29, 2009, from 3:00 to 5:00 UTC spanning event 18, which erupted at 3:23 UTC with a plume reaching up to 14.6 km elevation (Schneider and Hoblitt, this volume; Bull and Buurman, this volume). Comparing the skyplots with the tephra dispersion given by Bull et al. (2012), it appears that we face a very unfortunate satellite constellation with no signals traveling through the dense plume. The later, more evolved and dispersed plume seems not to affect the signal significantly.

The last skyplot in Fig. 17 covers the time of the large outlier at station DUMM on March 23, 2009, which shows up right at the beginning of the time series in Fig. 11 and coincides with event 01 at about 06:38 UTC (marked by arrow 'A'). RVBM and RBED are running at this time but lack this feature (compare to Figs. 10 and 12). Neither the phase residuals for individual satellites nor the RMS value in Fig. 11 indicates anything unusual for this epoch. Here, we assume an incorrectly resolved phase ambiguity or other problems with the solution caused this spike.

The DUMM time series in Fig. 11 contains one last distinctive feature that begins in the evening of April 3 and stops early on April 4 and remains unexplained (marked by arrow 'B'). No other station
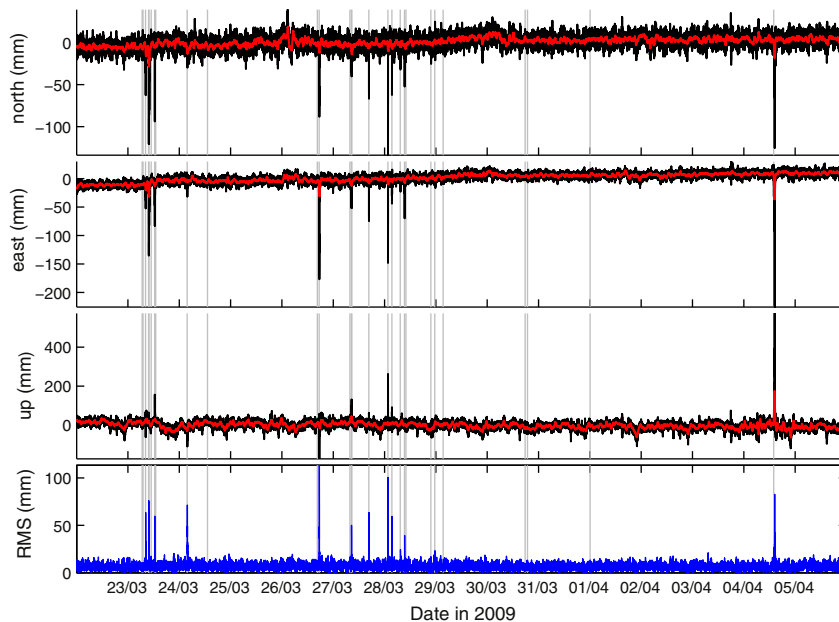
Fig. 10. RVBM positions with respect to AC17 from March 20 to April 5, 2009 (north, east, up, and RMS). Black lines are 30 s solutions, red lines are half-hour sliding window averages. Vertical gray lines indicate individual explosions (Table 1 in Bull and Buurman, this volume). Large plumes result in phase delay and hence position changes of RVBM due to phase delays for satellite–station combinations that cross the plume (Houlié et al., 2005a, 2005b). (For interpretation of the references to color in this figure legend, the reader is referred to the web version of this article.)
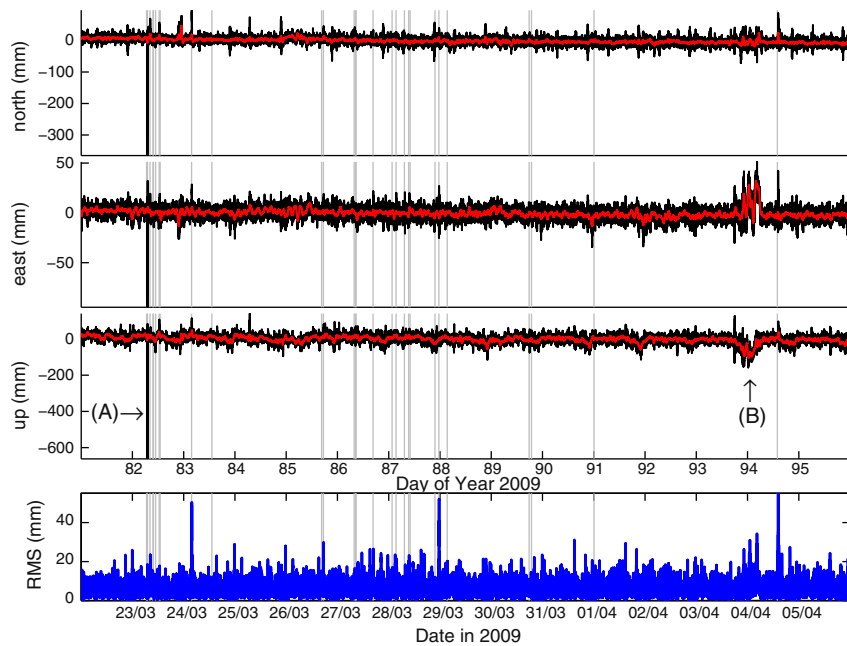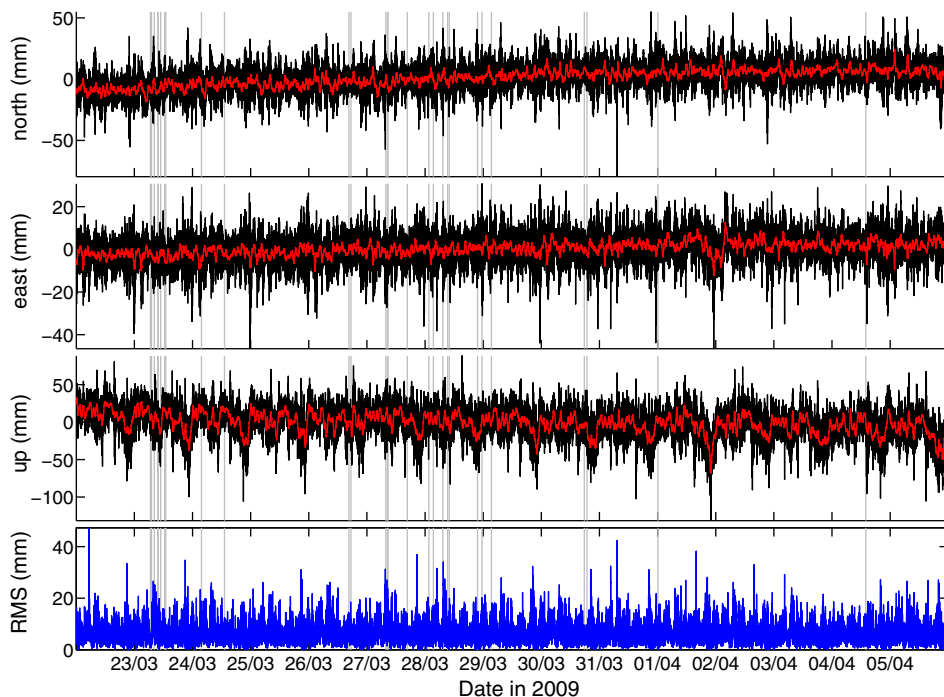
Fig. 11. Same as Fig. 10 but for station DUMM. Arrow (A) marks non-plume related spike on March 23, 2009. Arrow (B) marks unexplained deformation at the end of April 03 to April 04, 2009.

shows any similar deformation. Although an earthquake swarm occurred during this time (Buurman et al., this volume), it seems rather unlikely for this to cause such a deformation pattern. The phase residuals appear normal during this time and the pattern is inconsistent with subsurface migration of material, which we would expect to induce uplift first. Also such deformation would be seen at RVBM and RBED as well. From the amplitudes of the other days we can infer that this signal is too large to be multi-path. One possible explanation

is loading deformation due to a pulse of water/mud flowing down Drift River Valley.

6. Discussion

As explained in Section 2 and depicted in Fig. 1 (right), the data situation for the 2009 Redoubt eruption is not optimal and the measured volcanic deformation signals are not particularly large. This

Fig. 12. Same as Fig. 10 but for station RBED.
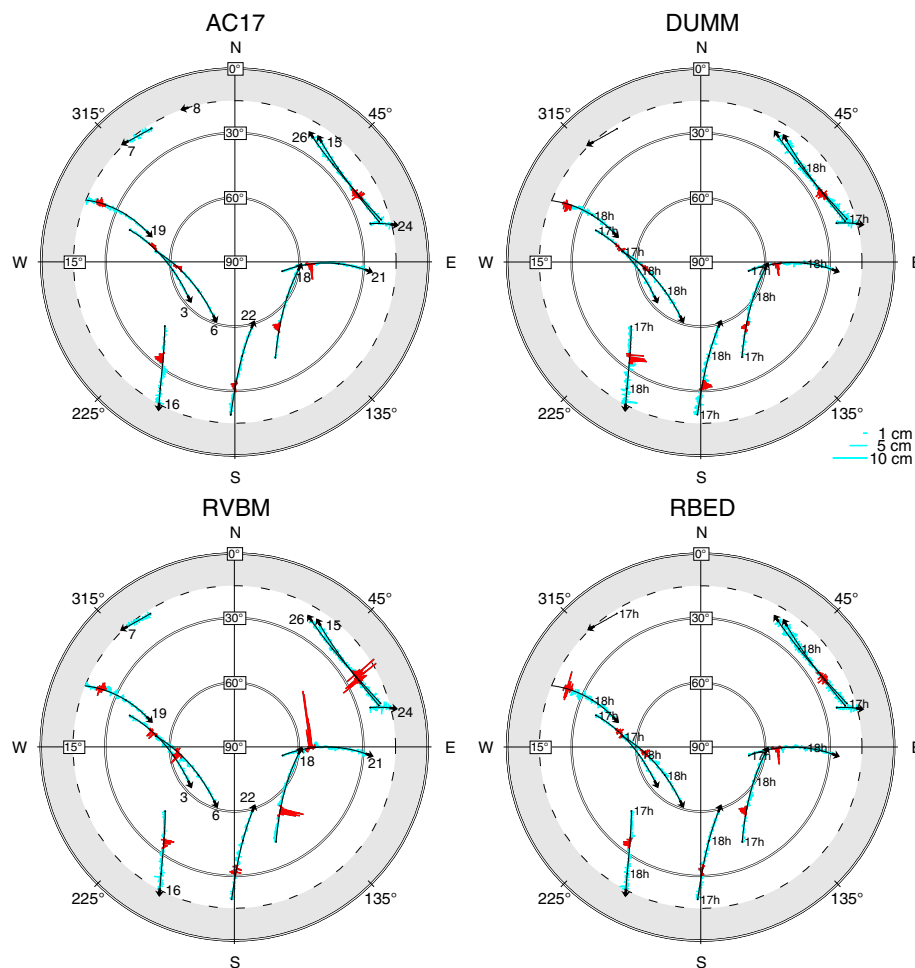
Fig. 13. Skyplot of phase residuals per satellite for AC17, DUMM, RVBM, RBED for March 26, 2009 from 17:00 to 18:30 UTC covering the time Event 18 occurred (17:24 UTC, Bull and Buurman (this volume)). The setup is similar for each of the subplots: the outer circle marks azimuths for the satellites and also indicates 0° of elevation above the horizon as seen from the station. The two inner circles mark 30°, 60° of elevation. 90° of elevation is directly above the station. Thin black lines indicate the tracks of the GPS satellites. The turquoise lines are the time series of phase residuals for this satellite. The red sections indicate the eruption time from 17:24 to 17:35 UTC. See text for detailed description on observations. Satellites are identified in the left column by PRN numbers at the end of the sky tracks next to a black arrow that points in the direction of motion of the satellite. The numbers next to black dots in the right column along those lines mark full UTC hours of the observation interval. (For interpretation of the references to color in this figure legend, the reader is referred to the web version of this article.)

limits our ability to discriminate between volcanic and non-volcanic signals (see, for example, Section 2), which is complicated by the lack of detailed data for processes dominating changes in hydrosphere and cryosphere in this remote region.

Splitting the signal into temporal phases affects the signal statistics (e.g., uncertainties increase), but the sum of displacements of the individual eruption phases is within the uncertainty of the displacements observed for the entire period. This argues that splitting the signal introduces only small errors in our source inversions. The difference seems to be driven mainly by the small signal to noise ratio for the precursory and effusive periods. However, we demonstrated in Section 5 that constraining the precursory source to a geometry that fits the data reasonably would have been impossible without investigating the phases separately and removing deflationary signals from the campaign data set.

While the F-Test provides a slight preference toward inflation of the prolate spheroid inferred from explosive deflation, we find the inflation of a Mogi source at the base of this spheroid to be an equally possible scenario driving precursory deformation. The horizontal offset between the precursory Mogi source and the prolate spheroid is negligible given the small signals and superimposed, unmodeled processes as well as the small offset over depth ratio. The sum of displacements of final source models for the individual eruption phases

(Table 3, bold) with either precursory source produces a good fit when compared to the large data set that includes displacements for the whole network spanning the time from summer 2008 to summer 2009 (Fig. 8D,F). Consequently, we provide both models as possible explanations for deformation during the precursory phase.

The source depths for both sources have large uncertainties associated with them, but locate in the general vicinity of each other (Table 3). The precursory Mogi source locates somewhat below the prolate spheroid making a case for magma influx at the spheroid's base. The prolate spheroid reaches up to shallower levels. It remains speculation whether this structure actually connects to a second small reservoir at 2–4.5 km bsl as suggested by, e.g., Coombs et al. (this volume) and Werner et al. (this volume). If a reservoir at these depths exists, the material removed must have been smaller than the network detection limit, e.g., about 0.002 km³ for a Mogi source (Fig. 3), which is an underestimate as we are not taking magma compressibility into account. Immediate replacement of material evacuated from such a source would be another possible explanation for the lack of measured deformation associated with a shallow reservoir.

The lack of measured deformation from 2001 to 2008 (Fig. 4) and apparent lack of deformation from 1991 to 2001, combined with only a small precursory inflation (Table 3) indicates that much of the material that erupted in 2009 had been in place prior to 2001 and
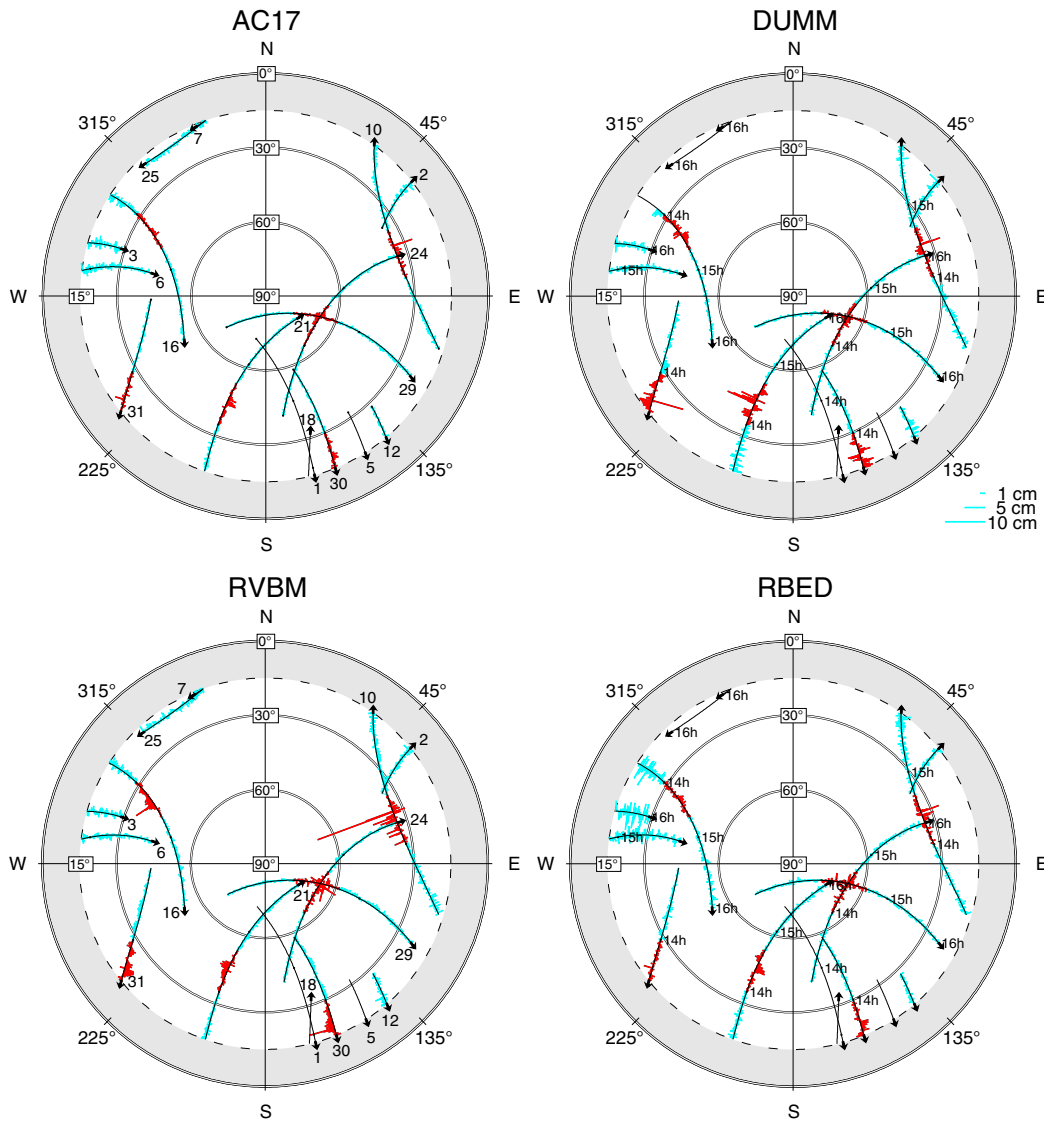
Fig. 14. Skyplot of phase residuals per satellite for AC17, DUMM, RVBM, RBED for April 04, 2009. Red sections indicate time of eruption from about 14:00–14:40 UTC. Fig. 13 describes the setup of this figure. (For interpretation of the references to color in this figure legend, the reader is referred to the web version of this article.)

probably prior to 1991. No new magma influx occurred until the onset of the precursory inflation beginning in May 2008. Although it is likely that the magma was leftover from the 1989–90 event, a more successful analysis of the 1991 GPS campaign data would be necessary to confirm this hypothesis.

Bull and Buurman (this volume) derive a total volume of erupted material between 0.08 and 0.12 km^3 which is about 1.5 times more than our best fit estimate for the explosive and effusive phases (0.0667 km^3). We have to keep in mind that the uncertainty intervals for the erupted volumes are large. Using the upper limits of erupted materials we can explain up to about 0.12 km^3 of erupted material; the upper limits of magma volume correspond to deeper limits of source depth. This indicates a very good agreement between geodetically derived volume estimates and the actual erupted volume, as our volume estimates assume incompressible magma. For Mount St. Helens, Mastin et al. (2008) report 3–4 times as much erupted volume as inferred intruded material while Voight et al. (2010) similarly suggest a ratio of 6 for incoming magma over geodetically measured reservoir wall volume change at Soufriére Hills Volcano. Bull and Buurman (this volume), however, found very low vesicularity (<10%) for the material erupted during the eruption. This reduces magma compressibility, which is mainly controlled by the presence

of bubbles due to exsolved gases in the magma. These gases may have escaped in the time since emplacement in 1989–90 or even before then.

The discrepancy in volume of the final dome as derived by Bull and Buurman (this volume) and Diefenbach et al. (this volume) (0.054 km^3) and our estimate of 0.0167 km^3 for the effusive phase may support the hypothesis of erupted material being drawn from a shallow 2–4.5 km reservoir (Coombs et al., this volume; Werner et al., this volume) and instantly replaced with fresh magma from depth. Decompression due to rise of the magma may account for the 3.2 times more voluminous erupted material (dense rock equivalent) at the surface, compared to the geodetically derived effusive volume.

7. Conclusions

This paper summarizes the geodetic observations during the 2009 Redoubt eruption and provides interpretations of these data. We investigate changes in long term time series of daily GPS positioning solutions to infer characteristics of the magmatic source feeding this event. Furthermore, we find a combination of kinematic position trajectories and satellite phase residuals plotted along satellite sky tracks
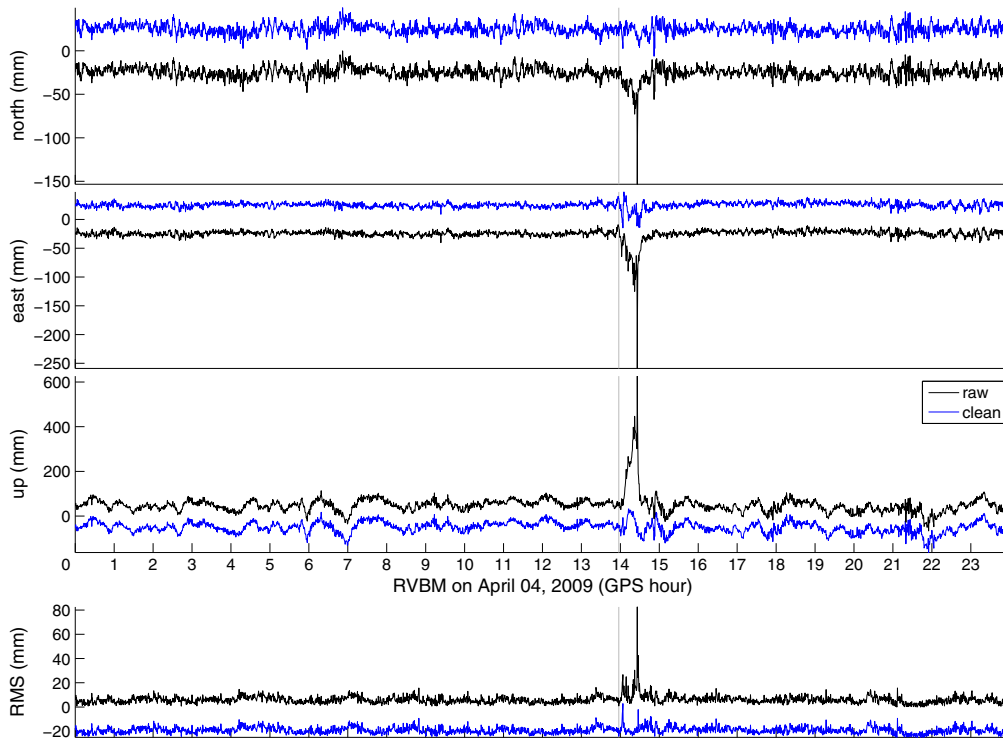
Fig. 15. Kinematic solution for RVBM on April 04, 2009 with AC17 as a base station. Black line is original solution, blue line shows position time series with satellite PRN 10 deleted from 14:00 to 14:45 GPS time (shifted for clarity). Clearly the spike in the position time series is reduced, as is the associated RMS value. Some scatter in the position remains which may be due to the other satellites being affected by the ash plume or actual ground motion associated with the eruption. (For interpretation of the references to color in this figure legend, the reader is referred to the web version of this article.)

as seen by individual GPS stations a helpful tool for eruption plume detection.

7.1. Magmatic process

We conclude that displacements due to a source in the mid-crustal region (7–13 km below sea level) beneath the final dome of the 2009 eruption are seen during all stages of the eruption. No deformation was observed during 2001–2008, until the start of the precursory phase. Detected pre-eruptive intrusion of new material at depth began as early as May 2008 at a steady rate (compare to deep long

period earthquakes below 20 km beginning in December 2008 discussed by Power et al. (this volume)). This culminated in a reversal of displacements during the explosive activity from March 23–April 4, 2009. Thus, the geodetic precursors to the eruption preceded any seismic precursors although they were not identified until later. Note that we do not see any deformation associated with evacuation of material before March 23, 2009, although a first explosion was reported for March 15, 2009 (Table 1 in Bull and Buurman, this volume). During the explosive phase and the effusive phase (April 5–June 1, 2009) we see a net loss of material from the storage region. This suggests that some of the erupted material was already in place
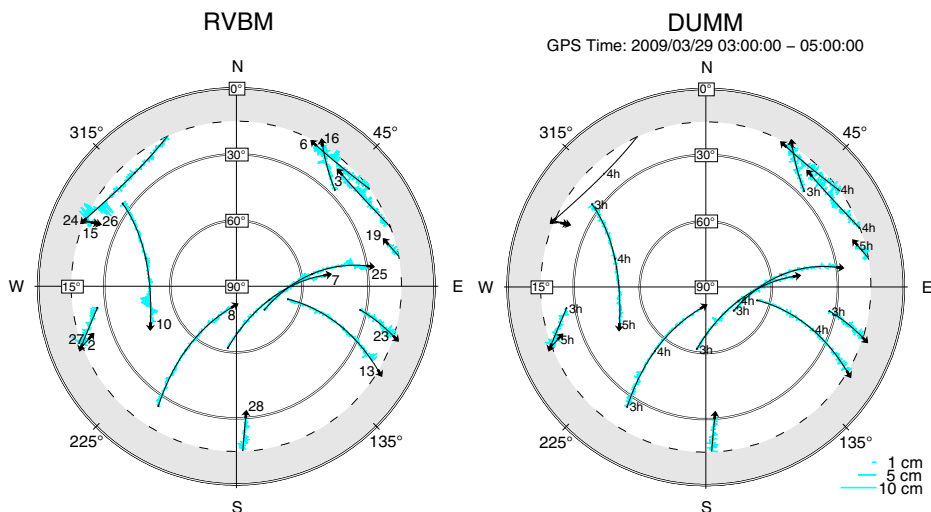
Fig. 16. Skyplot of phase residuals per satellite for DUMM and RVBM for March 29, 2009, Fig. 13 describes the setup of this figure. Event 18 (Bull and Buurman, this volume) occurs at 3:23 UTC with a plume extending to the NE.

Phase RMS at DUMM
GPS Time: 2009/03/23 05:59:00 – 2009/03/23 08:00:00
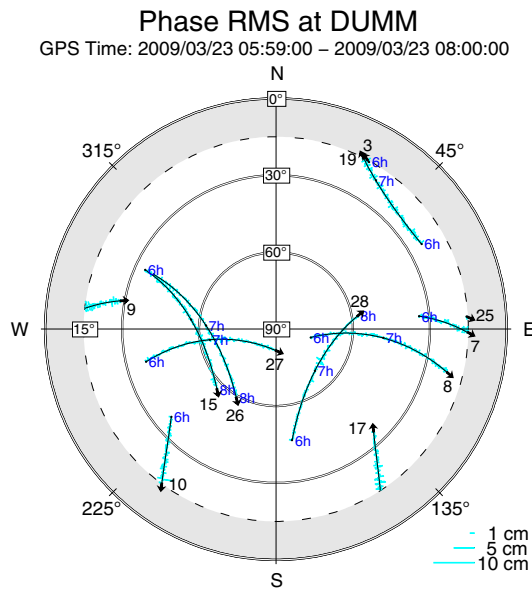
Fig. 17. Skyplot of phase residuals per satellite for DUMM for March 23, 2009, Fig. 13 describes the setup of this figure. The big spike in Fig. 11 coincides with event 01 at about 06:38 UTC, but is not associated with any unusual residuals.

or emplaced without being detected. One or all of the following processes could be responsible for this: (a) compensation of displacements due to smaller intrusions by ductile processes within the edifice, (b) intrusions of material prior to 2001, or (c) evacuation of left over material from the previous eruption in 1989–90.

Coombs et al. (this volume) suggest that unerupted hot, gas-rich magma heated and mobilized magmas residing in a shallow reservoir at 2–4.5 km bsl. We see possible deformation due to removal at these depths considering the uncertainty in location of the upper end of our suggested prolate spheroid. One hypothesis (Fig. 18) that ties deep seismicity (Power et al., this volume), petrology (Coombs et al., this volume), and our observations together is a two reservoir system in the mid- to shallow crust. Material from a diffuse magma source at 25–38 km (Power et al., this volume) flowed in at about 13 km depth beginning as early as May 2008. This reheated and remobilized residing material in the prolate spheroid from 7 to 11.5 km resulting in migration to shallower depth (2–4.5 km; Coombs et al. (this volume)). By end of January beginning of February 2009 shallow seismic tremor set on (Buurman et al., this volume) suggesting reheating

and remobilization of material residing in the shallower reservoir; allowing gases to pass. As this material, leftover from the 1989–90 event or earlier, extruded beginning on 23 March 2009, the mix of fresh and reheated material from the deeper stages of the system replaced it and made the shallow removal undetectable by geodesy. In this case, the resulting pressure/volume change reflects only the deeper source, which experienced net evacuation.

### 7.2. Ash plume detection in subdaily positioning solutions

We have related systematic spikes in subdaily positioning solutions to phase delays for station–satellite-pairs that cross dense parts of volcanic plumes. While the technique of detecting ash plumes with GPS has been described before by Houlié et al. (2005a, 2005b), this possibility seems not generally included in monitoring or data analysis efforts and is, in fact, not well explored. We show that plotting the phase residuals along the sky tracks of satellites provides easy access to plume azimuths. A high number of satellite–station pairs crossing a vent should be desired when geodetic networks for volcano deformation monitoring are designed. Kinematic solutions in near real-time could be used for plume sensing and verification and hence assist remote sensing efforts to fill some of the gaps created by slow satellite repeat times or cloud cover. From our results it is obvious that standard sampling rates of 15–30 s are sufficient to resolve the plume signal.

While intriguing, this certainly will not detect all plumes. We show that gaps in vent crossing station–satellite pairs may prohibit detection of plumes or ash concentrations may not be large enough to affect the signal significantly. Therefore, this technique should be seen as complementary to seismic and remote sensing monitoring.

Future work is necessary to determine ash concentrations and plume heights that affect the GPS signal quality significantly and hence determine detection limits. Results from such studies might in turn allow to estimate plume parameters such as density from GPS noise characteristics. Furthermore, reprocessing of any existing data set that indicates the existence of a plume with Ultra-rapid orbits or real time orbit products should clarify whether real time detection is feasible.

Acknowledgments
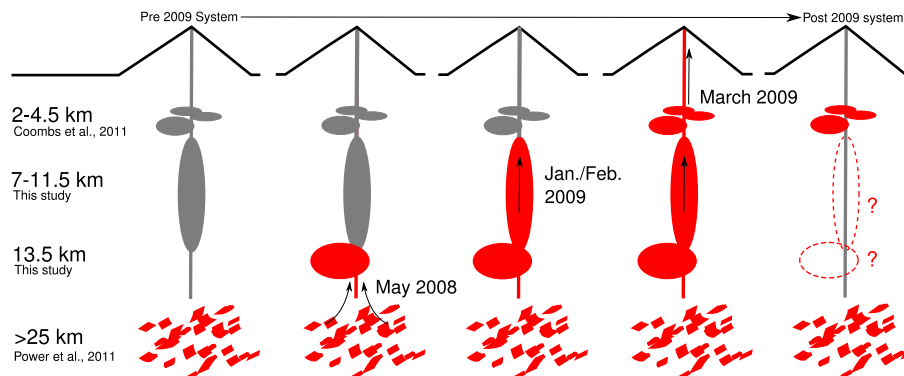
Fig. 18. Cartoon illustrating the evolution of the Redoubt Volcano plumbing system as suggested by geodetic, seismic, and petrologic data. Here we tie deep seismicity (Power et al., this volume), petrology (Coombs et al., this volume), and our observations together by proposing a two reservoir system in the mid- to shallow crust. Material from 25 to 38 km migrated to about 13 km depth beginning as early as May 2008; reheating and remobilizing residing material in the prolate spheroid from 7 to 11.5 km. This resulted in migration to 2–4.5 km depth (Coombs et al., this volume); supported by shallow seismic tremor beginning in January/February 2009 (Buurman et al., this volume). This material extruded from 23 March 2009 on. The mix of fresh and reheated material from the deeper stages of the system replaced extruded material and made the shallow removal undetectable by geodesy.

References

Anderson, E.M., 1936. The dynamics of the formation of cone-sheets, ring-dykes, and caldron-subsidences. Proceedings of the Royal Society of Edinburgh 56, 128–157.

Battaglia, M., Cervelli, P.F., Murra-Muraleda, J.R., 2012. Modeling Crustal Deformation: A Catalog of Deformation Models and Modeling Approaches.

Bleick, H.A., Coombs, M.L., Bull, K., Wessels, R. Volcano–ice interactions during the precursory phase of unrest preceding the 2009 eruption of Redoubt Volcano, Alaska. This volume.

Boehm, J., Niell, A., Tregoning, P., Schuh, H., 2006. Global Mapping Function (GMF): a new empirical mapping function based on numerical weather model data. Geophysical Research Letters 33, L07304.

Boehm, J., Heinkelmann, R., Schuh, H., 2007. Short note: a global model of pressure and temperature for geodetic applications. Journal of Geodesy 81, 679–683.

Bonaccorso, A., Davis, P.M., 1999. Models of ground deformation from vertical volcanic conduits with application to eruptions of Mount St. Helens and Mount Etna. Journal of Geophysical Research 104, 10531–10542.

Bull, K.F., Buurman, H. An overview of the 2009 eruption of Redoubt Volcano, Alaska. Journal of Volcanology and Geothermal Research this volume.

Bull, K.F., Cameron, C.E., Coombs, M.L., Diefenbach, A.K., Lopez, Taryn, McNutt, S.R., Neal, C.A., Payne, A.L., Power, J.A., Schneider, D.J., Scott, W.E., Snedigar, S.F., Thompson, Glenn, Wallace, K.L., Waythomas, C.F., Webley, P.W., Werner, C.A., 2012. The 2009 eruption of Redoubt Volcano, Alaska. In: Schaefer, J.R. (Ed.), Alaska Division of Geological & Geophysical Surveys Report of Investigation, 2011-5, 45 p.

Buurman, H., West, M.E., Thompson, G. Seismicity of the 2009 Redoubt Eruption. Journal of Volcanology and Geothermal Research this volume, in review.

Coombs, M., Sisson, T., Bleick, H., Henton, S., Nye, C., Payne, A., Cameron, C., Larsen, J., Wallace, K., Bull, K.F. Andesites of the 2009 eruption of Redoubt Volcano, Alaska. Journal of Volcanology and Geothermal Research this volume, in review.

Diefenbach, A., Bull, K.F., Wessels, R., McGimsey, R. Photogrammetric monitoring of lava dome growth during the 2009 eruption of Redoubt Volcano. Journal of Volcanology and Geothermal Research this volume, in review.

Dow, J.M., Neilan, R.E., Rizos, C., 2009. The International GNSS Service in a changing landscape of Global Navigation Satellite Systems. Journal of Geodesy 83, 191–198.

Dzurisin, D., 2003. A comprehensive approach to monitoring volcano deformation as a window on the eruption cycle. Reviews of Geophysics 1–29.

Estey, L.H., Meertens, C.M., 1999. TEQC: the multi-purpose toolkit for GPS / GLONASS data. GPS Solutions 3, 42–49.

Freymueller, J.T., Kaufman, A.M., 2010. Changes in the magma system during the 2008 eruption of Okmok volcano, Alaska, based on GPS measurements. Journal of Geophysical Research 115, B12415.

Freymueller, J.T., Woodard, H., Cohen, S.C., Cross, R., Elliott, J., Larsen, C.F., Hreinsdóttir, S., Zweck, C., 2008. Active deformation processes in Alaska, based on 15 years of GPS measurements. In: Freymueller, J.T., Haeussler, P.J., Wesson, R.L., Ekström, G. (Eds.), Active Tectonics and Seismic Potential of Alaska, AGU, pp. 1–42.

Fu, Y., Freymueller, J.T., van Dam, T., 2012. The effect of using inconsistent ocean tidal loading models on GPS coordinate solutions. Journal of Geodesy 86, 409–421. http://dx.doi.org/10.1007/s00190-011-0528-1.

Grapenthin, R., Sigmundsson, F., Geirsson, H., Árnadóttir, T., Pinel, V., 2006. Icelandic rhythmics: annual modulation of land elevation and plate spreading by snow load. Geophysical Research Letters 33, L24305.

Grapenthin, R., Sigmundsson, F., Ofeigsson, B.G., Sturkell, E., Hooper, A., 2010. Pressure sources versus surface loads: analyzing volcano deformation signal composition with an application to Hekla volcano, Iceland. Geophysical Research Letters 37, L20310.

Gregorius, T., 1996. GIPSY OASIS II: How It Works. Self. University of Newcastle upon Tyne.

Herring, T., King, R., McClusky, S., 2010. GAMIT-GLOBK Reference Manuals, Release 10.4.

Hilla, S., 2004. Plotting pseudorange multipath with respect to satellite azimuth and elevation. GPS Solutions 8, 44–48.

Houlié, N., Briole, P., Nercessian, A., Murakami, M., 2005a. Sounding the plume of the 18 August 2000 eruption of Miyakejima volcano (Japan) using GPS. Geophysical Research Letters 32, L05302.

Houlié, N., Briole, P., Nercessian, A., Murakami, M., 2005b. Volcanic plume above Mount St. Helens detected with GPS. Eos, Transactions, American Geophysical Union 86, 277–281.

Kouba, J., 2009. Testing of global pressure / temperature (GPT) model and global mapping function (GMF) in GPS analyses. Journal of Geodesy 83, 199–208.

Larson, K.M., Bilich, A., Axelrad, P., 2007. Improving the precision of high-rate GPS. Journal of Geophysical Research 112, B05422.

Masterlark, T., 2007. Magma intrusion and deformation predictions: sensitivities to the Mogi assumptions. Journal of Geophysical Research 112, B06419.

Mastin, B.L.G., Roeloffs, E., Beeler, N.M., Quick, J.E., 2008. Constraints on the size, overpressure, and volatile content of the Mount St. Helens magma system from geodetic and dome-growth measurements during the 2004–2006 eruption. U.S. Geological Survey Professional Paper, 1750, pp. 461–488. early 2006.

Miller, T.P., Chouet, B.A., 1994. The 1989–1990 eruptions of Redoubt Volcano, Alaska. Journal of Volcanology and Geothermal Research 62.

Mogi, K., 1958. Relations between eruptions of various volcanoes and the deformations of the ground surface around them. Bulletin of the Earthquake Research Institute, University of Tokyo 36, 99–134.

Newman, A.V., Dixon, T.H., Gourmelen, N., 2006. A four-dimensional viscoelastic deformation model for Long Valley Caldera, California, between 1995 and 2000. Journal of Volcanology and Geothermal Research 150, 244–269.

Paul, F., 2010. GLIMS Glacier Database. National Snow and Ice Data Center/World Data Center for Glaciology, Boulder, CO. Digital Media.

Pinel, V., Sigmundsson, F., Sturkell, E., Geirsson, H., Einarsson, P., Gudmundsson, M.T., Högnadóttir, T., 2007. Discriminating volcano deformation due to magma movements and variable surface loads: application to Katla subglacial volcano, Iceland. Geophysical Journal International 169, 325–338.

Power, J., Stihler, S., Haney, M. Seismic observations of Redoubt Volcano, Alaska 1989–2010 and a conceptual model of the Redoubt magmatic system. Journal of Volcanology and Geothermal Research this volume, in review.

Press, W.H., Teukolsy, S.A., Vetterling, W.T., Flannery, B.P., 2007. Numerical Recipes: The Art of Scientific Computing, 3rd edition. Cambridge University Press.

Reed, B.L., Lanphere, M.A., Miller, T.P., 1992. Double glacier volcano, a 'new' Quaternary volcano in the eastern Aleutian volcanic arc. Bulletin of Volcanology 54, 631–637.

Schneider, D., Hoblitt, R. Doppler weather observations of the 2009 eruption of Redoubt Volcano, Alaska. Journal of Volcanology and Geothermal Research this volume, in review.

Segall, P., 2010. Earthquake and Volcano Deformation. Princeton University Press, Princeton.

Sigmundsson, F., 2006. Iceland Geodynamics, Crustal Deformation and Divergent Plate Tectonics. Springer-Praxis, Chichester, UK.

Suito, H., Freymueller, J.T., 2009. A viscoelastic and afterslip postseismic deformation model for the 1964 Alaska earthquake. Journal of Geophysical Research 114, B11404.

Turcotte, D.L., Schubert, G., 2002. Geodynamics. Cambridge University Press.

Voight, B., Widiwijayanti, C., Mattioli, G., Elsworth, D., Hidayat, D., Strutt, M., 2010. Magma-sponge hypothesis and stratovolcanoes: case for a compressible reservoir and quasi-steady deep influx at Soufrière Hills Volcano, Montserrat. Geophysical Research Letters 37, L00E05.

Waythomas, C., Pierson, T., Major, J. Lahar and flowage hazards in the Drift River Valley associated with the 2009 eruption of Redoubt Volcano, Alaska. Journal of Volcanology and Geothermal Research this volume, in review.

Webley, P.W., Lopez, T.M., Dean, K.G., Rinkleff, P., Dehn, J., Cahill, C.F., Wessels, R.L., Schneider, D.J., Ekstrand, A., Bailey, J.E., Izbekov, P., Worden, A. Remote observations of eruptive clouds and surface thermal activity during the 2009 eruption of Redoubt Volcano. Journal of Volcanology and Geothermal Research, this volume, in review.

Werner, C., Kelly, P., Doukas, M., Lopez, T., Pfeffer, M., McGimsey, R.G., Neal, C.A. Degassing associated with the 2009 Eruption of Redoubt Volcano, Alaska. This volume.

Wessel, P., Smith, W.H.F., 1995. New version of the Generic Mapping Tools released. Eos, Transactions, American Geophysical Union.

Yamakawa, N., 1955. On the strain produced in a semi-infinite elastic solid by an interior source of stress. Zisin (Journal of the Seismological Society of Japan) 84–98.

Yang, X.M., Davis, P.M., Dieterich, J.H., 1988. Deformation from inflation of a dipping finite prolate spheroid in an elastic half-space as a model for volcanic stressing. Journal of Geophysical Research 93, 4257–4549.

Zumberge, J.F., Heflin, M.B., Jefferson, D.C., Watkins, M.M., Webb, F.H., 1997. Precise point positioning for the efficient and robust analysis of GPS data from large networks. Journal of Geophysical Research 102, 5005–5017.